https://doi.org/10.5194/egusphere-2024-1361
Preprint. Discussion started: 20 June 2024


# Forecasting contrail climate forcing for flight planning and air traffic management applications: The CocipGrid model in pycontrails 0.51.0

Zebediah Engberg[1], Roger Teoh[2], Tristan Abbott[1], Thomas Dean[1], Marc E.J. Stettler[2], and Marc L. Shapiro[1]

[1]Breakthrough Energy, 4110 Carillon Point, Kirkland, WA 98033, United States
[2]Department of Civil and Environmental Engineering, Imperial College London, London, SW7 2AZ, United Kingdom

*Correspondence to*: Marc Shapiro (marc.shapiro@breakthroughenergy.org)

**Abstract.** The global annual mean contrail net radiative forcing may exceed that of aviation's cumulative $CO_2$ emissions by at least two-fold. As only around 2-3% of all flights are likely responsible for 80% of the global annual contrail climate forcing, re-routing these flights could reduce the formation of strongly warming contrails. Here, we develop a contrail forecasting model that produces global predictions of persistent contrail formation and their associated climate forcing. This model builds on the methods of the existing contrail cirrus prediction model (CoCiP) to efficiently evaluate infinitesimal contrail segments initialized at each point in a regular 4D spatiotemporal grid until their end-of-life. Outputs are reported in a concise meteorology data format that integrates with existing flight planning and air traffic management workflows. This "grid-based" CoCiP is used to conduct a global contrail simulation for 2019 to compare with previous work and analyze spatial trends related to strongly warming/cooling contrails. We explore two approaches for integrating contrail forecasts into existing flight planning and air traffic management systems: (i) using contrail forcing as an additional cost parameter within a flight trajectory optimizer; or (ii) constructing polygons of airspace volumes with strongly-warming contrails to avoid. We demonstrate a probabilistic formulation of the grid-based model by running a Monte Carlo simulation with ensemble meteorology to mask grid cells with significant uncertainties in the simulated contrail climate forcing. This study establishes a working standard for incorporating contrail mitigation within existing flight planning and management workflows and demonstrates how forecasting uncertainty can be incorporated to minimize unintended consequences associated with increased $CO_2$ emissions of avoidance.

## 1 Introduction

Global aviation activity produces significant socio-economic benefits, but also emits $CO_2$ and non-$CO_2$ pollutants that impact the environment in the form of climate change and air quality degradation. Lee et al. (2021) estimated that aviation accounted for 3.5% of the global anthropogenic climate forcing in 2018, where the collective effective radiative forcing

https://doi.org/10.5194/egusphere-2024-1361
Preprint. Discussion started: 20 June 2024


(ERF) from non-$CO_2$ components such as contrail cirrus (57.4 [17, 98] mW $m^{-2}$ at a 95% confidence interval) and nitrogen oxides (17.5 [0.6, 29] mW $m^{-2}$) could be two times larger than its cumulative $CO_2$ emitted since the 1940s (34.3 [28, 40] mW $m^{-2}$). Given the significant impact from aviation non-$CO_2$ emissions, the European Union (EU) Emissions Trading System's (ETS) Monitoring Reporting and Verification framework has recently been amended to require flights travelling within Europe to measure their non-$CO_2$ impacts, including the effects from contrail cirrus, from 2025 onwards (European Commission, 2023).

Contrails form behind an aircraft when conditions in the rapidly cooling exhaust plume become supersaturated with respect to water, enabling water vapor to condense on the surface of particles to form droplets that subsequently freeze into ice particles (Kärcher and Yu, 2009; Schumann, 1996). Previous studies have estimated that up to 85% of contrails are short-lived and sublimate within five minutes (Teoh et al., 2023; Wolf et al., 2023b). The remaining contrails typically persist in ice supersaturated regions (ISSR), where they can evolve into contrail cirrus clusters that become indistinguishable from natural cirrus (Haywood et al., 2009). These persistent contrails exhibit lifetimes that generally follow a negative exponential distribution with a mean duration of 1–3 h (Caiazzo et al., 2017; Teoh et al., 2023; Vázquez-Navarro et al., 2015). Persistent contrails always induce a localised warming effect by absorbing and re-emitting outgoing longwave (LW) infrared radiation. They can also cause a cooling effect during daylight hours by reflecting incoming shortwave (SW) solar radiation back to space (Meerkötter et al., 1999). Contrail LW and SW instantaneous radiative forcing (RF) varies regionally and influenced by air traffic density, aircraft-engine particle number emissions, background radiation fields, ambient meteorology, and diurnal and seasonal factors (Kärcher, 2018; Schumann and Heymsfield, 2017; Teoh et al., 2022a, 2023).

Observational tools such as satellite imagery and ground-based cameras offer the means to monitor contrail formation and early evolution (Duda et al., 2019; Mannstein et al., 2010; Rosenow et al., 2023; Schumann et al., 2013b; Vázquez-Navarro et al., 2015), but they are currently unable to determine the RF over a contrail's lifetime. To simulate the full contrail lifecycle and climate forcing, earlier studies have relied on physics-based modelling approaches, including large-eddy simulations (LES) (Lewellen, 2014; Lewellen et al., 2014; Unterstrasser, 2016) and parameterised Lagrangian models such as the Contrail Cirrus Prediction Model (CoCiP) (Schumann, 2012), Contrail Evolution and Radiation Model (CERM) (Caiazzo et al., 2017), and Aircraft Plume Chemistry, Emissions, and Microphysics Model (APCEMM) (Fritz et al., 2020). Contrails have also been parameterized in general circulation models (GCMs) to capture the physical processes of the atmosphere and longer-range spatiotemporal feedback (Bier and Burkhardt, 2022; Chen and Gettelman, 2013; Ponater et al., 2021).

Recently, Teoh et al. (2023) used CoCiP to simulate contrails globally for 2019, estimating that around 20% of all flights produced persistent contrails. Among these persistent contrail-forming flights, 70% of them (17% of all flights) had a net warming effect and 10% of them (2.7% of all flights) were responsible for 80% of the global annual contrail energy forcing

https://doi.org/10.5194/egusphere-2024-1361
Preprint. Discussion started: 20 June 2024


($EF_{contrail}$; i.e., the cumulative contrail climate forcing over its lifetime). These findings highlight a potential pathway for aviation to reduce its overall climate forcing by strategically re-routing a small subset of flights to minimise the formation of strongly warming contrails (Teoh et al., 2020b, a; Wilhelm et al., 2021). While two small-scale operational contrail avoidance trials have been conducted in recent years (American Airlines, 2023; Lokman, 2022), several challenges must be addressed to implement a contrail-minimisation strategy at a larger-scale. Such challenges include the: (i) integration of a contrail forecast model into flight planning and management software to optimize flight trajectories; (ii) automation of operational procedures to perform trajectory adjustments (Lokman, 2022; Molloy et al., 2022); and (iii) inclusion of meteorological and contrail forecast uncertainties in the decision-making framework for contrail mitigation actions (Agarwal et al., 2022; Gierens et al., 2020; Molloy et al., 2022). All three challenges can effectively be addressed if the contrail climate forcing forecasts can be provided in a format similar to turbulence forecasts (Turbli, 2024), so that they can be readily integrated into the operational workflow of existing flight planning software (Martin Frias et al., 2024).

In a collaboration between DLR, Imperial College, and Breakthrough Energy, CoCiP was implemented in Python and released open-source in the `pycontrails` library in 2023 (Shapiro et al., 2023). This study builds on the existing trajectory-based CoCiP as implemented and versioned in `pycontrails` to create a prototype contrail forecasting model (`CocipGrid`) capable of generating global predictions of persistent contrail formation and their associated climate forcing. It aims to compare the simulated contrail climate forcing and its spatial trends provided by the forecasting model with those derived from the trajectory-based CoCiP and earlier global contrail simulation studies. We demonstrate the contrail forecasting model in flight trajectory optimization and propose strategies to account for contrail forecast uncertainties arising from weather forecasts and model simplifications. The `CocipGrid` model is implemented and versioned in the `pycontrails` library alongside the existing CoCiP model (version v0.51.0 at the time of writing).

The contrail forecasting strategy is based in a Lagrangian model instead of LES and GCMs because it can most efficiently compute the $EF_{contrail}$ using reanalysis or forecast meteorology provided by numerical weather prediction (NWP) models. While we expect contrail forecasts to evolve as modelling and observational capabilities improve, we aim to use this prototype to enable stakeholders (e.g., flight planners and air navigation service providers) to accommodate contrail forecasts in flight planning by establishing standards, data integration and modifications to software tools and operational processes.

## 2 Trajectory-based CoCiP

CoCiP simulates the contrail properties and climate forcing for a single flight trajectory using inputs of: (i) flight trajectory waypoints; (ii) fuel properties, such as the water vapour emissions index ($EI_{H_2O}$) and lower calorific value ($Q_{fuel}$); (iii) aircraft properties and performance parameters, including the true airspeed ($V_{TAS}$), fuel mass flow rate ($\dot{m}_f$), overall

https://doi.org/10.5194/egusphere-2024-1361
Preprint. Discussion started: 20 June 2024


efficiency (η), aircraft mass, and wingspan; (iv) aircraft-engine specific non-volatile particulate matter (nvPM) number emissions index ($EI_n$); and (v) historical or forecast meteorology provided by NWP models (Schumann, 2012).

Briefly, CoCiP utilises the Schmidt-Appleman criterion (SAC) to estimate the threshold temperature for contrail formation ($T_{SAC}$), where $T_{SAC}$ is influenced by η, $EI_{H_2O}$, and $Q_{fuel}$ (Schumann, 1996). For waypoints that satisfy the SAC i.e., with ambient temperature ($T_{amb}$) falling below $T_{SAC}$, CoCiP simulates the wake vortex downwash using a probabilistic two-phase wake vortex decay model which parametrically estimates the mean downward displacement and initial contrail width and depth as a function of aircraft mass, wingspan, and $V_{TAS}$ (Holzapfel, 2003). Persistent contrail segments are defined when the post-wake vortex contrail ice water content (IWC) in two consecutive waypoints is greater than $10^{-12}$ kg kg$^{-1}$. For each contrail segment, the contrail ice crystal number per flight distance flown ($n_{ice,initial}$) is initialized by estimating the nvPM particle number emissions per flight distance flown, fraction of nvPM particles that activates to form contrail ice crystals ($f_{activation}$), and fraction of contrail ice crystals that survive the wake-vortex phase ($f_{surv}$),

$$n_{\mathrm{ice,initial}} = \mathrm{nvPM\ EI_n} \times \dot{m}_{\mathrm{f,dist}} \times f_{\mathrm{activation}} \times f_{\mathrm{surv}}, \text{ where} \quad (1)$$

$$f_{\mathrm{activation}} = -0.661\mathrm{e}^{(T_{\mathrm{amb}} - T_{\mathrm{SAC}})} + 1, \text{ and} \quad (2)$$

$$f_{\mathrm{surv}} = \frac{\mathrm{IWC_{initial}} - \Delta\mathrm{IWC_{ad}}}{\mathrm{IWC_{initial}}}. \quad (3)$$

The nvPM number emissions per unit distance is calculated by multiplying the aircraft-engine specific nvPM $EI_n$ with the fuel consumption per distance flown ($\dot{m}_{f,dist}$), $f_{activation}$ is determined by the difference between $T_{amb}$ and $T_{SAC}$ (Bräuer et al., 2021; Teoh et al., 2022a), and $f_{surv}$ is assumed to be proportional to the change in contrail IWC due to adiabatic heating from the wake vortex downwash ($\Delta IWC_{ad}$) (Schumann, 2012).

For persistent contrail segments, a Runge-Kutta scheme simulates the evolution of their locations, dimensions, and properties, with model time steps ($dt$, < 3600 s; 300 s in this study), until their end-of-life, defined as when the contrail segment age exceeds a maximum lifetime of 12 h, ice particle number per volume of air drops below $10^3$ m$^{-3}$, or optical depth ($\tau_{contrail}$) falls below $10^{-6}$ (Schumann, 2012; Teoh et al., 2023). At each time step, a parametric RF model estimates the local contrail SW and LW RF (RF', the change in radiative flux over the contrail coverage area) (Schumann et al., 2012), and the $EF_{contrail}$ is estimated by multiplying local contrail net RF' by its contrail segment length ($L$) and width ($W$) and integrated over its lifetime ($t_{max}$) (Schumann et al., 2011),

$$\mathrm{EF_{contrail}\ [J]} = \int_0^{t_{\max}} \mathrm{RF'_{net}}(t) \times L(t) \times W(t)\, \mathrm{d}t. \quad (4)$$

The estimated $RF'_{net}$ and $EF_{contrail}$ account for the presence of natural cirrus above/below the contrail (Schumann et al., 2012), and recent CoCiP studies have further formulated an approach to approximate the change in contrail $RF'_{net}$ due to contrail-contrail overlapping (Schumann et al., 2021; Teoh et al., 2023). For this study, we note that the contrail diffusivity, ice

https://doi.org/10.5194/egusphere-2024-1361
Preprint. Discussion started: 20 June 2024


crystal loss rate, lifetime, and climate forcing are sensitive to the contrail segment angle (α, the angle between the contrail segment and the longitudinal axis) because α influences the magnitude of wind shear acting normal to the contrail segment ($\frac{dS_n}{dZ}$) (Schumann, 2012),

$$\frac{dS_n}{dZ} = \frac{dV}{dZ}\cos(\alpha) - \frac{dU}{dZ}\sin(\alpha), \quad (5)$$

where $\frac{dV}{dZ}$ and $\frac{dU}{dZ}$ are the magnitude of wind shear acting on the eastward and northward direction respectively.

Previous studies have shown that the range of simulated contrail properties from CoCiP are generally consistent when compared with in situ measurements, remote sensing, and satellite observations (Jeßberger et al., 2013; Schumann et al., 2017, 2021; Schumann and Heymsfield, 2017; Teoh et al., 2023). For further details on the versioning and evolution of the trajectory-based CoCiP, readers can refer to Appendix A1 and the documentation of the open-source `pycontrails` library (Shapiro et al., 2023).

## 3 Grid-based CoCiP

The existing implementation of CoCiP described in Section 2, i.e., the trajectory-based CoCiP, simulates contrails formed along a flight path. However, when used to optimize the trajectory of multiple flights, the trajectory-based approach becomes computationally inefficient because of the need for repeated model re-runs across each flight and various trajectory iterations to identify the solution with minimum $EF_{contrail}$. One way to address this limitation is to produce a 4D field of the $EF_{contrail}$ per flight distance flown, effectively identifying regions forecast to form persistent warming contrails. We achieve this by extending the trajectory-based CoCiP to a grid-based approach, where an infinitesimal contrail segment is: (i) initialized at each point in a 4D spatiotemporal domain; (ii) simulated until its end of life with a d$t$ of 300 s using the equations of the trajectory-based CoCiP; and (iii) has its cumulative climate forcing attributed back to the grid cell where it originally formed. The output from this approach takes the same form as traditional 4D NWP data.

Table 1 presents the differences between the trajectory- and grid-based CoCiP. The primary distinction lies in how the contrail segment properties are initialized. Here, we describe our methodology to initialize the contrail segment properties in the grid-based CoCiP (Section 3.1) the meteorological datasets used in this study (Section 3.2), and outline key differences in the grid-based CoCiP when it is configured to run with a nominal (Section 3.3) and a Monte Carlo simulation (Section 3.4).

### 3.1 Initial contrail properties

In the trajectory-based CoCiP, contrail segment properties are initialized based on the flight segment (α and $V_{TAS}$) and aircraft-engine specific properties (wingspan, aircraft mass, $\dot{m}_f$, η, and nvPM $EI_n$). However, this approach cannot be directly

https://doi.org/10.5194/egusphere-2024-1361
Preprint. Discussion started: 20 June 2024


applied to the grid-based CoCiP because of the need to: (i) model aircraft performance ($V_{TAS}$, $\dot{m}_f$, aircraft mass, η, and nvPM $EI_n$) locally, rather than based on entire flight trajectories; and (ii) determine an appropriate value for α, which influences the wind shear acting on the contrail segment, c.f. Eq. (5), without prior information about direction-of-travel.

Moreover, the grid-based CoCiP must account for variations in aircraft performance across different aircraft and engine types that are known to influence the $EF_{contrail}$ (Teoh et al., 2022a). In theory, this issue could be resolved by re-running the grid-based CoCiP for each aircraft-engine combination. However, this method would lead to increased computational and data transfer requirements, as well as increased operational complexity when used in the context of flight planning and execution. Instead, we address this challenge by classifying the most-commonly used passenger aircraft-engine types into $N$ number of groups based on their similarities in aircraft mass and nvPM $EI_n$ (Tables 2 and 3), thereby introducing a fifth dimension to the model outputs (longitude × latitude × altitude × time × $N$ aircraft-engine group).

**Table 1: Summary of the key differences between the trajectory-based and grid-based CoCiP.**

| | Trajectory-based CoCiP | Grid-based CoCiP |
|---|---|---|
| **Flight segments** | Flight segments are initialized based on the flight trajectory, which is provided as a sequence of flight waypoints. | An infinitesimal flight segment is initialized at each point in a 4D spatiotemporal grid (longitude, latitude, altitude, and time). |
| **Aircraft-engine performance and emissions** | • Requires the specification of aircraft and engine type for each flight,<br>• Aircraft performance at each waypoint is estimated using aircraft performance models based on information about entire flight trajectories,<br>• The nvPM $EI_n$ at each waypoint is estimated using the nvPM emissions profile provided by the ICAO aircraft engine emissions databank (EDB) and the $T_4/T_2$ methodology. | • The most-commonly used passenger aircraft-engine types are classified based on their similarities in aircraft mass and nvPM $EI_n$, and the model is run for each aircraft-engine group.<br>• For each aircraft-engine group, input parameters for aircraft performance and emissions model are:<br>i. Set to parameters for the aircraft-engine type with largest market share in the group (nominal simulation), or<br>ii. Estimated from an empirical multivariate distribution (Monte Carlo simulation, see Fig. 1).<br>• Aircraft performance at each waypoint is estimated using a variant of the Poll-Schumann (PS) model that can be run for a single point rather than entire flight trajectories, and nvPM $EI_n$ is estimated using the same methodology as trajectory-based CoCiP. |
| **Contrail initialisation** | The initial contrail properties (i.e., contrail dimensions, ice crystal number, and contrail segment angle) depends on the provided aircraft-engine properties, performance, and emissions. | The initial contrail dimensions and ice crystal number is initialized using the equations from the trajectory-based CoCiP. However, the contrail segment angle is undefined in the grid-based CoCiP and is either:<br>i. Treated as a calibrated parameter that maximises the agreement between the trajectory-based and grid-based CoCiP (nominal simulation), or<br>ii. Assumed to be uniformly distributed between 0 and 360° (Monte Carlo simulation). |
| **Model outputs** | Cumulative $EF_{contrail}$ over the contrail segment | 4D $EF_{contrail}$ per flight distance, cumulated over the |

https://doi.org/10.5194/egusphere-2024-1361
Preprint. Discussion started: 20 June 2024


| | | |
|---|---|---|
| | lifetime, attributed back to the flight segment where the contrails were first formed. | contrail segment lifetime and attributed back to the original grid cell. |
| **Relevant applications** | • Estimating the $EF_{contrail}$ from the provided flight trajectories.<br>• Calculating historical estimates of the global/regional annual mean contrail net RF.<br>• Performing flight trajectory optimisation for single/multiple flights to minimise persistent contrail formation/$EF_{contrail}$. | • Generating maps to identify regions forecast to form persistent warming and cooling contrails.<br>• Improving computational efficiency in flight trajectory optimisation for a fleet of aircraft compared to the trajectory-based CoCiP. |

**Table 2: Classification of commonly used passenger aircraft-engine types into 12 unique groups based on their similarities in aircraft mass and nvPM $EI_n$. The aircraft types listed here are labelled based on their ICAO aircraft type designator.**

| Aircraft-engine classification | | nvPM $EI_n$ | | |
|---|---|---|---|---|
| | | **Low** | **Nominal** | **High** |
| **Aircraft mass** | **Light** | • A19N (LEAP-1A)<br>• A20N (LEAP-1A)<br>• A21N (LEAP-1A)<br>• B38M (LEAP-1B) | • A319 (CFM56)<br>• A320 (CFM56)<br>• A321 (CFM56)<br>• B737 (CFM56)<br>• B738 (CFM56)<br>• B739 (CFM56) | • A19N (Pratt & Whitney)<br>• A20N (Pratt & Whitney)<br>• A21N (Pratt & Whitney)<br>• A319 (IAE V2500)<br>• A320 (IAE V2500)<br>• A321 (IAE V2500) |
| | **Intermediate** | N/A | • B752 (RB211)<br>• B753 (RB211)<br>• B762 (CF6-80E)<br>• B763 (CF6-80E) | N/A |
| | **Medium** | • B788 (GEnx)<br>• B789 (Genx)<br>• B78X (Genx) | • A342 (CFM56/Trent500)<br>• A343 (CFM56/Trent500)<br>• A345 (CFM56/Trent500)<br>• A346 (CFM56/Trent500)<br>• B788 (Trent 1000)<br>• B789 (Trent 1000)<br>• B78X (Trent 1000) | • A332 (Trent 700/CF6-80E)<br>• A333 (Trent 700/CF6-80E) |
| | **Heavy** | • B772 (GE90)<br>• B773 (GE90)<br>• B77L (GE90)<br>• B77W (GE90) | • A359 (Trent XWB)<br>• A35K (Trent XWB) | N/A |
| | **Super heavy** | • B748 (Genx) | • A388 (Trent 900) | • B742 (CF6-80C)<br>• B743 (CF6-80C)<br>• B744 (CF6-80C) |

The classification by aircraft mass and nvPM is informed by the strong correlation between the nvPM emissions per flight distance, which is estimated as a product of nvPM $EI_n$ and $\dot{m}_f$ (where the aircraft mass is used as a proxy), and the $EF_{contrail}$ per flight distance (R = 0.71) (Teoh et al., 2022a). While a higher *N* is expected to improve the agreement between the

https://doi.org/10.5194/egusphere-2024-1361
Preprint. Discussion started: 20 June 2024


trajectory- and grid-based CoCiP, our goal is to identify an acceptable minimum value for $N$ to reduce the computational demands and operational complexity in practice (Section 4). For each group, the waypoint-specific inputs (α, $V_{TAS}$, wingspan, aircraft mass, $\dot{m}_f$, η, and nvPM $EI_n$) vary depending on whether the grid-based CoCiP is configured to run in a nominal mode (Section 3.3) or with a Monte Carlo simulation (Section 3.4).

### 3.2 Meteorology

In practice, the grid-based CoCiP would utilise forecast meteorological products (e.g. the European Centre for Medium-Range Weather Forecasts (ECMWF) Atmospheric Model high resolution 10-day forecast (ECMWF, 2024) to provide contrail climate forcing forecasts. For this paper, we use historical meteorology, specifically the ECMWF ERA5 High Resolution Realisation (HRES) Reanalysis for the nominal simulation and the ERA5 10-member ensembles for the Monte Carlo simulation (Section 3.4) (Hersbach et al., 2020).

Both datasets share a vertical resolution of 26 model levels, spanning from 6,300 m (20,000 feet) to 15,000 m (49,000 feet), but the ERA5 HRES Reanalysis offers a higher spatiotemporal resolution (0.25° longitude × 0.25° latitude at a 1 h temporal resolution) than the ERA5 10-member ensembles (0.5° longitude × 0.5° latitude at a 3 h temporal resolution). The spatiotemporal resolution of the grid-based CoCiP is adjustable and set to align with the ERA5 HRES Reanalysis. For both meteorological products, we apply a correction to ensure that the ERA5 RHi distribution is consistent with in-situ measurements (refer to Appendix A2 for further details) (Teoh et al., 2023).

**Table 3: Summary of the aircraft properties (wingspan, service ceiling altitude, and maximum Mach number) and range of aircraft performance and emissions parameters (aircraft mass, η, and nvPM $EI_n$) for the 12 aircraft-engine groups. Details of the aircraft-engine types that are included in each group can be found in Table 2.**

| Aircraft-engine properties and performance parameters | | nvPM $EI_n$ | | |
|---|---|---|---|---|
| | | **Low** | **Nominal** | **High** |
| **Aircraft mass** | **Light** | • Mass: 55,000 – 80,000 kg<br>• nvPM $EI_n$: 1 ×$10^{11}$ $kg^{-1}$<br>• η: 0.20 – 0.26<br>• Wingspan: 34 – 36 m<br>• Max altitude: 41,000 ft.<br>• Max Mach: 0.82 | • Mass: 55,000 – 80,000 kg<br>• nvPM $EI_n$: (0.8 – 1.0) ×$10^{15}$ $kg^{-1}$<br>• η: 0.20 – 0.26<br>• Wingspan: 34.1 – 34.3 m<br>• Max altitude: 41,000 ft.<br>• Max Mach: 0.82 | • Mass: 55,000 – 80,000 kg<br>• nvPM $EI_n$: (2 – 4) ×$10^{15}$ $kg^{-1}$<br>• η: 0.20 – 0.26<br>• Wingspan: 34 – 36 m<br>• Max altitude: 41,000 ft.<br>• Max Mach: 0.82 |
| | **Intermediate** | N/A | • Mass: 85,000 – 160,000 kg<br>• nvPM $EI_n$: (0.6 – 1.2) ×$10^{15}$ $kg^{-1}$<br>• η: 0.21 – 0.26<br>• Wingspan: 38.0 – 47.6 m<br>• Max altitude: 43,100 ft.<br>• Max Mach: 0.86 | N/A |
| | **Medium** | • Mass: 165,000 – 240,000 kg<br>• nvPM $EI_n$: 1 ×$10^{11}$ $kg^{-1}$<br>• η: 0.30 – 0.34<br>• Wingspan: 60.1 m<br>• Max altitude: 43,100 ft.<br>• Max Mach: 0.90 | • Mass: 165,000 – 250,000 kg<br>• nvPM $EI_n$: (4 – 7) ×$10^{14}$ $kg^{-1}$<br>• η: 0.29 – 0.33<br>• Wingspan: 60.1 – 60.3 m<br>• Max altitude: 43,100 ft.<br>• Max Mach: 0.86 – 0.90 | • Mass: 160,000 – 210,000 kg<br>• nvPM $EI_n$: (0.7 – 1) ×$10^{15}$ $kg^{-1}$<br>• η: 0.25 – 0.28<br>• Wingspan: 60.3 m<br>• Max altitude: 41,000 ft.<br>• Max Mach: 0.86 |
| | **Heavy** | • Mass: 200,000 – 320,000 kg | • Mass: 205,000 – 250,000 kg | N/A |

https://doi.org/10.5194/egusphere-2024-1361
Preprint. Discussion started: 20 June 2024


| | | | | |
|---|---|---|---|---|
| | | • nvPM $EI_n$: (3 – 4) ×$10^{14}$ $kg^{-1}$<br>• η: 0.28 – 0.30<br>• Wingspan: 64.8 m<br>• Max altitude: 43,100 ft.<br>• Max Mach: 0.89 | • nvPM $EI_n$: (5 – 8) ×$10^{14}$ $kg^{-1}$<br>• η: 0.33 – 0.35<br>• Wingspan: 64.7 m<br>• Max altitude: 43,100 ft.<br>• Max Mach: 0.89 | |
| | **Super heavy** | • Mass: 275,000 – 400,000 kg<br>• nvPM $EI_n$: 1 ×$10^{11}$ $kg^{-1}$<br>• η: 0.32 – 0.34<br>• Wingspan: 68.4 m<br>• Max altitude: 42,100 ft.<br>• Max Mach: 0.90 | • Mass: 385,000 – 512,000 kg<br>• nvPM $EI_n$: (5 – 7) ×$10^{14}$ $kg^{-1}$<br>• η: 0.33 – 0.35<br>• Wingspan: 79.8 m<br>• Max altitude: 43,100 ft.<br>• Max Mach: 0.89 | • Mass: 250,000 – 360,000 kg<br>• nvPM $EI_n$: (6 – 8) ×$10^{14}$ $kg^{-1}$<br>• η: 0.27 – 0.29<br>• Wingspan: 64.4 m<br>• Max altitude: 45,000 ft.<br>• Max Mach: 0.92 |

### 3.3 Nominal simulation

Each aircraft-engine type is characterised by a set of fixed properties, including the: (i) wingspan; (ii) design-optimum Mach number; (iii) aerodynamic coefficients; and (iv) nvPM emissions profile, all of which are required as inputs to aircraft performance and emission models. Inputs (i) to (iii) are provided by the Poll-Schumann (PS) aircraft performance model (Poll and Schumann, 2020, 2021); while input (iv) is provided by the ICAO Aircraft Engine Emissions Databank (EASA, 2021). For each aircraft-engine group, which encompasses multiple aircraft-engine types (Table 2), we set these fixed properties to values of the aircraft-engine type with largest market share within the group (Teoh et al., 2024).

For waypoint-specific parameters (i.e., $V_{TAS}$, aircraft mass, $\dot{m}_f$, η, and nvPM $EI_n$), the nominal grid-based CoCiP obtains these parameters by assuming that the: (i) Mach number at each grid cell is equal to the design-optimum Mach number plus 0.04 to reflect real-world operational conditions (Teoh et al., 2024); (ii) aircraft mass at each altitude is equal to the value that maximises η; and using the (iii) PS aircraft performance model to estimate the $\dot{m}_f$ (Poll and Schumann, 2020, 2021); and (iv) $T_4/T_2$ methodology to estimate the nvPM $EI_n$ (EASA, 2021; Teoh et al., 2024). Assumption (i) is justified by the tendency of airlines to fly faster than the design-optimum conditions to minimise time-dependent costs and/or catch up with delays (Edwards et al., 2016; Lovegren and Hansman, 2011), while assumption (ii) is based on the rationale that a lower aircraft mass is required for the aircraft to cruise at higher altitudes (Fig. 1).

https://doi.org/10.5194/egusphere-2024-1361
Preprint. Discussion started: 20 June 2024


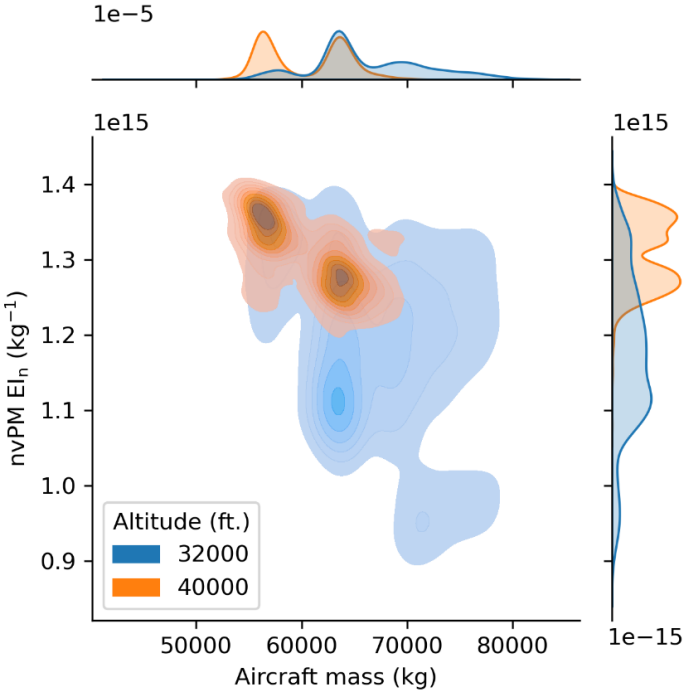


**Figure 1: The multivariate distribution of aircraft mass and nvPM $EI_n$ for one aircraft-engine group (light aircraft mass, and nominal nvPM $EI_n$) at 32,000 feet (in blue) and 40,000 feet (in orange).**

As α cannot be defined for an infinitesimal flight segment, the nominal grid-based CoCiP adopts a workaround by calibrating Eq. (5) as follows,

$$\frac{dS_n}{dZ} = f_{shear} \times \frac{dS}{dZ}, \text{ where} \quad (6)$$

$$\frac{dS}{dZ} = \sqrt{\left(\frac{dU}{dZ}\right)^2 + \left(\frac{dV}{dZ}\right)^2}, \quad (7)$$

$\frac{dS}{dZ}$ is the magnitude of the wind shear and $f_{shear}$ is a free parameter and has physical limits of 0 (i.e., contrail segment aligned with the wind shear) and 1 (i.e., contrail segment perpendicular to shear). We calibrate $f_{shear}$ = 0.665 by minimizing each of the error metrics when evaluating $EF_{contrail}$ from the trajectory- and grid-based CoCiP (described in Section 4).

### 3.4 Monte Carlo simulation

The grid-based CoCiP is set up to run in Monte Carlo simulations to explore the uncertainties related to model simplifications (i.e., aircraft-engine groups and the treatment of α) and meteorological forecasts. For each aircraft-engine group, we account for the multi-collinearity between different aircraft performance parameters (i.e., $V_{TAS}$, $M$, $\dot{m}_f$, η, and nvPM $EI_n$) by constructing an empirical multivariate distribution for each group to sample the required aircraft performance

https://doi.org/10.5194/egusphere-2024-1361
Preprint. Discussion started: 20 June 2024


parameters (Fig. 1). More specifically, the empirical multivariate distributions are derived using flight waypoints at the cruise phase of flight (i.e., above 25,000 feet and zero vertical climb rate) from the 2019 Global Aviation emissions Inventory based on ADS-B (GAIA) (Teoh et al., 2024).

Our Monte Carlo approach is based on a similar study investigating the contribution of the uncertainties related to the CoCiP input and model parameters on the contrail climate forcing (Platt et al., 2024). It involves conducting 100 separate global simulations, during which each of the ERA5 10-member ensembles remains fixed for 10 consecutive simulation runs. Within each of these 10 simulation runs, the aircraft performance parameters (i.e., $V_{TAS}$, aircraft mass, $\dot{m}_f$, η, and nvPM $EI_n$) at different altitudes are drawn from the empirical multivariate distribution (Fig. 1) and α is sampled from a uniform distribution that ranges between 0° and 360°. This setup yields a total of 10 ensemble members that capture the meteorological uncertainties, multiplied by 10 independent simulations that capture the variabilities in aircraft performance and α. These outputs are subsequently used to quantify the range of $EF_{contrail}$ per flight distance attributable to each grid cell and their respective probabilities of forming persistent warming/cooling contrails.

## 4 Comparing trajectory vs. grid-based CoCiP

Here, we use both the trajectory-based and (nominal) grid-based CoCiP to simulate the $EF_{contrail}$ from historical flight trajectories provided by GAIA (Teoh et al., 2024). We evaluate the agreement between both models and explore the trade-off between the model agreement and model simplification, i.e., formulating the grid-based CoCiP with a smaller number of aircraft-engine groups ($N$) as discussed in Section 3.1. To achieve these goals, we classify the most-commonly used passenger aircraft-engine types into groups of between 1 (no differentiation between aircraft-engine types) and 12 based on their aircraft mass and nvPM $EI_n$ (see Tables 2 and 3, and Appendix A3). We then filter the GAIA dataset to only include the 43 aircraft-engine types covered in Table 2 and randomly sample one day per week throughout the entire year of 2019. We extract flight waypoint data within each day and simulate the $EF_{contrail}$ using both the trajectory-based ($EF^{traj}_{contrail}$) and grid-based CoCiP ($EF^{grid}_{contrail}$).

Our goal in this analysis is not to validate grid-based CoCiP in an absolute sense, but to demonstrate that the grid-based CoCiP can provide sufficiently accurate representations of the trajectory-based CoCiP. We recognize the critical importance of validating both CoCiP variants against independent observations, which is an active area of ongoing research.

### 4.1 Metrics

The agreement between $EF^{traj}_{contrail}$ and $EF^{grid}_{contrail}$ is assessed using five distinct approaches. Together, these approaches are aimed at quantifying both the point-wise errors and fleet-aggregated errors. We note that these metrics are predominantly

https://doi.org/10.5194/egusphere-2024-1361
Preprint. Discussion started: 20 June 2024


biased towards evaluating the model's ability to correctly predict strongly warming contrails rather than all contrails, consistent with existing proposals that aim to target the 2-3% of flights that are responsible for 80% of the global annual $EF_{contrail}$ (Teoh et al., 2020b, a, 2023; Wilhelm et al., 2021).

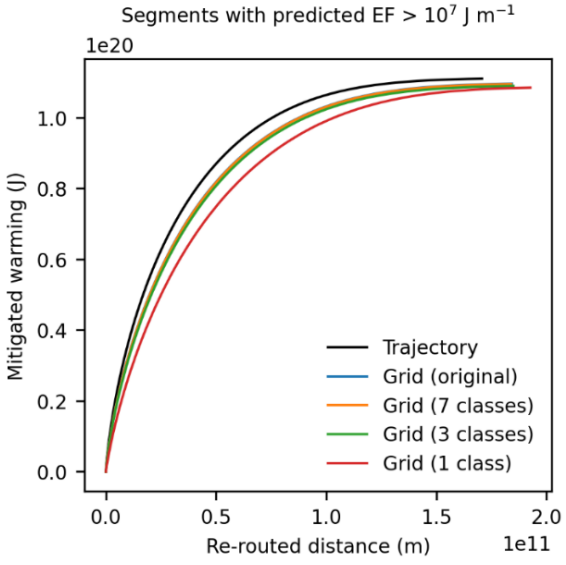


**Figure 2: Performance curves for the trajectory-based CoCiP (black line) and the grid-based CoCiP when it is configured using the exact/original aircraft-engine types (i.e., the same as the trajectory-based CoCiP; blue line), and with *N*=7 (orange line), *N*=3 (green line), and *N*=1 (red line) aircraft-engine groups respectively. Further methodological information used to construct these performance curves can be found in Appendix A4.**

Point-wise errors are quantified using three metrics including the false negative rate i.e. $P\left[\left(EF_{contrail}^{grid} < EF_{threshold}\right) \middle| \left(EF_{contrail}^{traj} > EF_{threshold}\right)\right]$, the false alarm rate $P\left[\left(EF_{contrail}^{traj} < EF_{threshold}\right) \middle| \left(EF_{contrail}^{grid} > EF_{threshold}\right)\right]$, and the modified mean absolute log error (modified-MALE). The false negative and false alarm rates serve to evaluate the accuracy of the grid-based CoCiP in identifying the location of moderately and strongly warming contrails, which are assumed to be those with an $EF_{threshold}$ of 1 $\times 10^7$ J m$^{-1}$ (around the 50$^{th}$ percentile) and 5 $\times 10^8$ J m$^{-1}$ (80$^{th}$ percentile) respectively (Teoh et al., 2023). In addition, the modified-MALE measures the average relative error between $EF_{contrail}^{traj}$ and $EF_{contrail}^{grid}$ at each flight segment, while minimising the impact of prediction errors in segments with a weak contrail climate forcing (i.e., $EF_{contrail} < 10^7$ J m$^{-1}$).

https://doi.org/10.5194/egusphere-2024-1361
Preprint. Discussion started: 20 June 2024


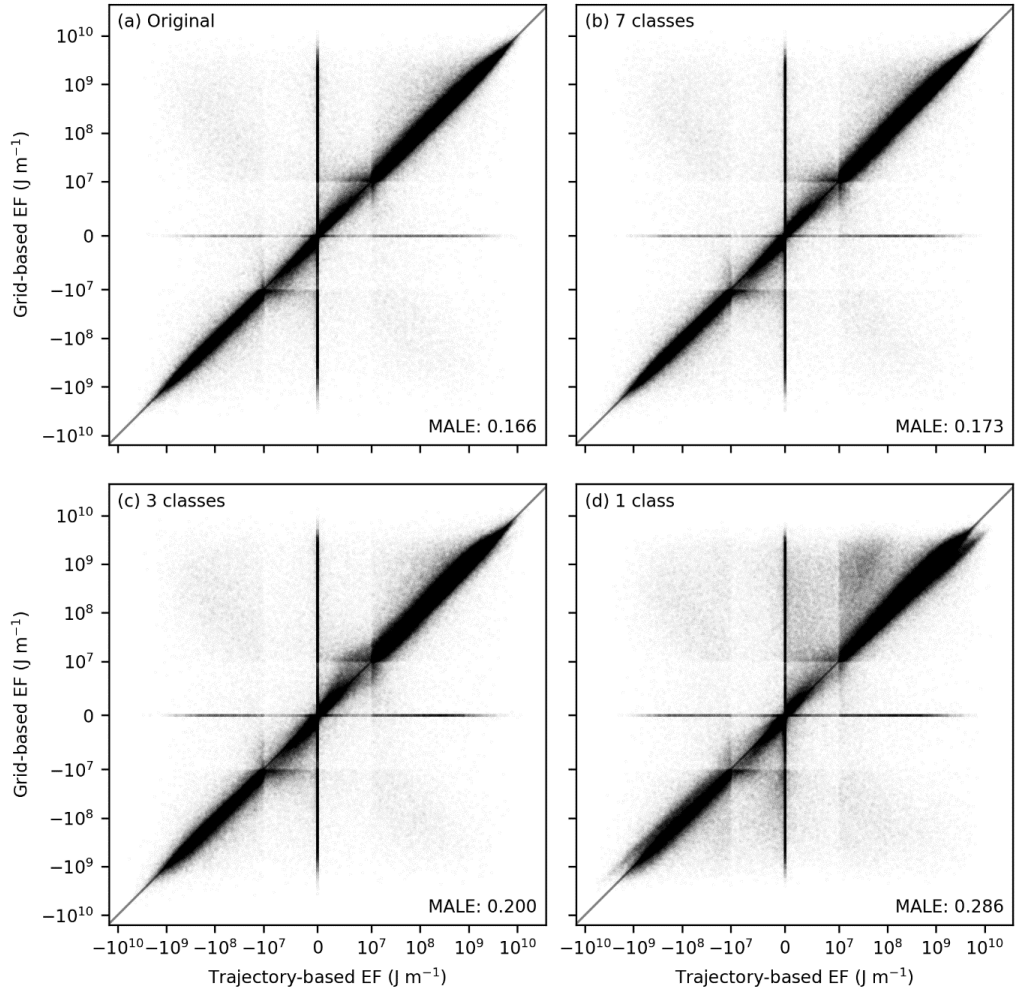


**Figure 3: Pointwise errors between $EF^{traj}_{contrail}$ and $EF^{grid}_{contrail}$ when the grid-based CoCiP is configured: (a) using the exact/original aircraft-engine types (i.e., the same as the trajectory-based CoCiP); and with (b) *N*=7; (c) *N*=3; and (d) *N*=1 aircraft-engine groups respectively. Each panel contains 10,000,000 randomly-sampled flight waypoints. The axes use a logarithmic scale for $|EF_{contrail}| > 10^{7}$ J m$^{-1}$ and a linear scale between $10^{-7}$ and $10^{7}$ J m$^{-1}$.**

Fleet-aggregated errors are evaluated using the weighted Kendall rank correlation coefficient ($\tau_w$), which assesses the grid-based CoCiP's capability to correctly rank flight segments by their magnitude of $EF^{traj}_{contrail}$. We additionally use two custom performance curve metrics that evaluate the deterioration in contrail mitigation potential when interventions are informed by imperfect predictions ($EF^{grid}_{contrail}$) (Platt et al., 2024). The performance curves are constructed by first sorting the flight segments based on an estimate of their $EF_{contrail}$ ($EF^{grid}_{contrail}$) and then plotting their cumulative $EF_{contrail}$ as a function of the cumulative flight distance flown ($L$), shown in Fig. 2. This is equivalent to a curve showing the reduction in $EF_{contrail}$ as a function of $L$, with interventions being prioritised based on an estimate of the $EF_{contrail}$ and assuming that the contrail mitigation at the flight segment is successful ($EF_{contrail}$ = 0). The cumulative $EF_{contrail}$ increases most quickly with the

https://doi.org/10.5194/egusphere-2024-1361
Preprint. Discussion started: 20 June 2024


cumulative $L$ if the $EF_{contrail}$ is based on perfect information (i.e., $EF^{traj}_{contrail}$) and less quickly if the $EF_{contrail}$ estimates (i.e., $EF^{grid}_{contrail}$) contain errors. We use these performance curves to quantify the: (i) change in initial mitigation rate (i.e., the reduced effectiveness in mitigating flight segments with the most strongly warming contrails), which is estimated from the gradient of a secant line over the first 5% of the cumulative $EF_{contrail}$ ($m_5$) and expressed as a ratio $\frac{m_5^{grid}}{m_5^{traj}} (< 1)$; and (ii) change in flight segment ratio, $\frac{L_{80}^{grid}}{L_{80}^{traj}} (> 1)$, which quantifies the additional flight distance where interventions have to be applied to mitigate 80% of the total $EF_{contrail}$. A detailed description of each metric can be found in Appendix A4.

### 4.2 Model comparison

Table 4 summarises the performance metrics when comparing the model agreement between the trajectory-based CoCiP and various configurations of the grid-based CoCiP, i.e., using the original aircraft-engine type for each flight as in the trajectory-based CoCiP, and with different aircraft-engine groupings ($1 \leq N \leq 12$), as outlined in Section 3 and Appendix A3. The performance metrics for the original aircraft-engine grouping show: (i) false negative and false alarm rates of 3.2% and 10.4% respectively when evaluated against moderately warming contrails ($EF_{threshold}$ = 1 ×$10^7$ J $m^{-1}$), and 6.0% and 17.7% respectively when assessed against strongly warming contrails ($EF_{threshold}$ = 5 ×$10^8$ J $m^{-1}$); (ii) a modified-MALE of 0.166, corresponding to a 47% relative error between $EF^{traj}_{contrail}$ and $EF^{grid}_{contrail}$; (iii) $\tau_w$ of 0.821, indicating a strong correlation between the rankings of $EF^{traj}_{contrail}$ and $EF^{grid}_{contrail}$; (iv) a change in the initial mitigation rate of 0.816, suggesting an 18% reduction in the effectiveness of mitigating the most strongly warming contrails with the grid-based CoCiP; and (v) a change in the flight segment ratio of 1.156, indicating that interventions must be applied to an additional 16% of the total flight distance flown to mitigate 80% of the $EF_{contrail}$.

Using different aircraft-engine groupings ($1 \leq N \leq 12$) rather than the original aircraft-engine type introduces additional sources of error between the trajectory-based and grid-based CoCiP (Table 4, and Fig. 2 and 3). The mean error across different performance metrics for $N$ = 12 and $N$ = 7 are around 0.6% and 2.8% relative to the configuration without any aircraft-engine grouping, but the degradation rate generally starts to increase when $N$ < 7. Specifically, the mean error for $N$ = 1 (34.5%) is around an order of magnitude larger than that of $N$ = 7 (2.8%), with these errors primarily arising from overestimates in the $EF_{contrail}$ from aircraft-engine types with low nvPM $EI_n$ (c.f. top right quadrant in Fig. 3d). Notably, a reduction from $N$ = 4 to $N$ = 3 results in an improvement in mean error across the performance metrics from 18.0% to 13.1%. This improvement can be attributed to the fact that $N$ = 3 categorises the aircraft-engine types solely based on their nvPM $EI_n$, whereas $N$ = 4 categorised the aircraft-engine types into two nvPM and two aircraft mass categories, thereby suggesting that the nvPM $EI_n$ is a stronger predictor of $EF_{contrail}$ than aircraft mass.

https://doi.org/10.5194/egusphere-2024-1361
Preprint. Discussion started: 20 June 2024


**Table 4: Summary of the different performance metrics used to evaluate the agreement between the grid-based CoCiP with different configurations of aircraft-engine groups (*N*) relative to the trajectory-based CoCiP. Further information on these metrics can be found in Section 4.1 and Appendix A4.**

| Number of aircraft-engine groups (*N*) | $EF_{threshold} = 10^7$ J m$^{-1}$ | | $EF_{threshold} = 5 \times 10^8$ J m$^{-1}$ | | Modified-MALE[a] | $\tau_w$[b] | Performance curves | | Mean error across all metrics[c] |
|---|---|---|---|---|---|---|---|---|---|
| | False negative | False alarm | False negative | False alarm | | | Initial mitigation rate | Flight segment ratios | |
| Original | 3.2% | 10.4% | 6.0% | 17.7% | 0.166 | 0.821 | 0.816 | 1.156 | - |
| 12 | 3.2% | 10.6% | 5.7% | 18.3% | 0.169 | 0.819 | 0.811 | 1.158 | **0.6%** |
| 7 | 3.6% | 10.7% | 5.7% | 18.6% | 0.173 | 0.814 | 0.809 | 1.160 | **2.8%** |
| 6 | 3.7% | 10.4% | 8.0% | 18.1% | 0.178 | 0.802 | 0.808 | 1.177 | **7.8%** |
| 5 | 3.8% | 11.0% | 9.5% | 18.0% | 0.183 | 0.790 | 0.787 | 1.202 | **11.7%** |
| 4 | 4.1% | 11.2% | 13.2% | 17.3% | 0.194 | 0.766 | 0.586 | 1.236 | **18.0%** |
| 3 | 4.7% | 12.2% | 5.6% | 22.0% | 0.201 | 0.784 | 0.791 | 1.191 | **13.1%** |
| 2 | 5.0% | 12.4% | 9.5% | 21.6% | 0.213 | 0.755 | 0.588 | 1.242 | **19.7%** |
| 1 | 5.1% | 16.0% | 9.5% | 29.4% | 0.286 | 0.670 | 0.526 | 1.378 | **34.5%** |

[a]: The modified mean absolute log error (modified-MALE), where a value of zero indicates perfect agreement in the magnitude of $EF_{contrail}$ between the trajectory-based and grid-based CoCiP, while larger values are indicative of larger relative errors. The modified-MALE can be converted to a percentage relative error using the following formula, $\text{Percentage relative error} = 100 \times (10^{\text{modified MALE}} - 1)$. A value of 1 implies that, on average, $EF^{grid}_{contrail}$ are off by one order of magnitude.

[b]: The weighted Kendall rank correlation coefficient ($\tau_w$), where $\tau_w = 1$ indicates a perfect agreement between the rankings of $EF^{traj}_{contrail}$ and $EF^{grid}_{contrail}$, $\tau_w = 0$ indicates a completely random relationship, while $\tau_w = -1$ indicates a perfect disagreement.

[c]: The mean percentage error across all performance metrics when compared with the grid-based CoCiP without any aircraft-engine configuration.

Based on these results, we draw three key insights to inform the selection of an optimal *N*: (i) the model agreement between the trajectory-based and grid-based CoCiP is comparable for $N = 12$ and $N = 7$, which suggests that there may not be a significant advantage to running the grid-based CoCiP with $N = 12$ rather than $N = 7$; (ii) $N = 3$, which categorises the aircraft-engine types solely based on nvPM $EI_n$, offers a reasonable trade-off between model accuracy and operational complexity; and (iii) $N = 1$ significantly degrades the accuracy of the grid-based CoCiP and is not recommended for operational use.

https://doi.org/10.5194/egusphere-2024-1361
Preprint. Discussion started: 20 June 2024


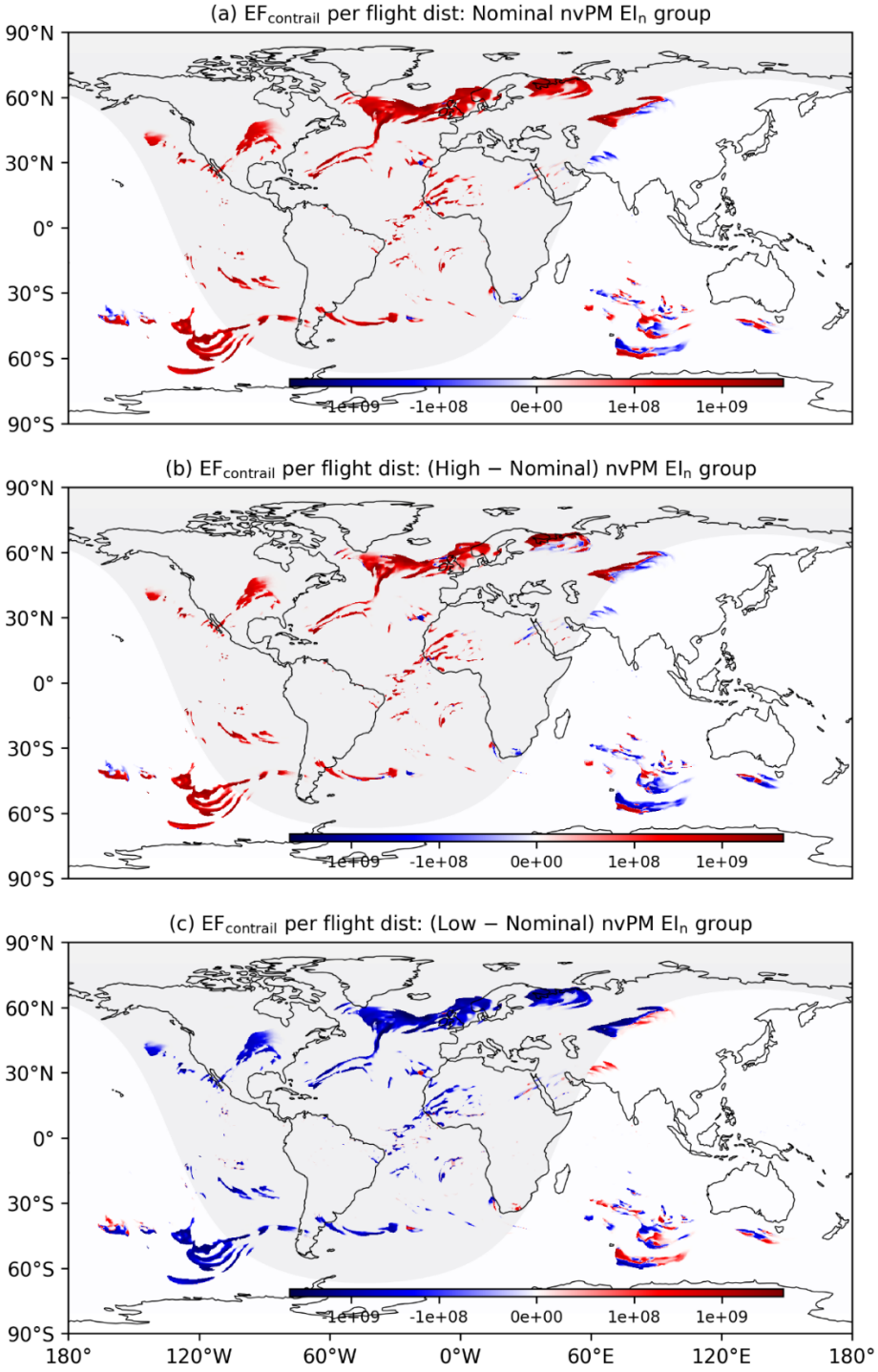


335 **Figure 4: The (a) absolute EF$_{contrail}$ per flight distance for the aircraft-engine group with nominal nvPM; and the absolute difference in EF$_{contrail}$ per flight distance between the (b) nominal and high nvPM aircraft-engine group; and (c) nominal and low nvPM aircraft-engine group. The global contrail climate forcing shown here are simulated at FL360 (10,973 m) on the 7$^{th}$ of January 2019 at 03:00:00. Basemap plotted using Cartopy 0.22.0 and sourced from Natural Earth; licensed under public domain.**

https://doi.org/10.5194/egusphere-2024-1361
Preprint. Discussion started: 20 June 2024


## 5 Application of grid-based CoCiP

Here, we run a 2019 full year grid-based global contrail simulation with $N = 3$ and reanalysis meteorology to quantify the annual statistics and spatial occurrence of strongly warming and cooling contrails (Section 5.1). We then introduce two different approaches for integrating the grid-based CoCiP into flight trajectory optimization (Section 5.2), followed by proposing two strategies to account for uncertainties within the decision-making process of contrail mitigation to increase the probability of achieving a net climate benefit (Section 5.3).

### 5.1 Global contrail simulation

The grid-based CoCiP produces a global map of the $EF_{contrail}$ per flight distance for each of the three aircraft-engine group that were categorised based on their nvPM $EI_n$ (Fig. 4 and Section 4.2). A comparison between the nominal and high nvPM aircraft-engine group (Fig. 4b) showed notable differences in the magnitude of $EF_{contrail}$, where the global mean $EF_{contrail}$ per flight distance for the high nvPM aircraft-engine group ($10.4 \times 10^8$ J m$^{-1}$) is around two times larger than the nominal nvPM group ($5.54 \times 10^8$ J m$^{-1}$). These groups also show differences in the sign of $EF_{contrail}$, especially at around 25–60°S and 60–150°E, where the number of grid cells with cooling contrails ($EF_{contrail} < 0$) in the high nvPM group is 18% more than the nominal nvPM group. These trends can be linked to the relationship between the nvPM $EI_n$ and contrail lifetime, where a larger nvPM $EI_n$ generally leads to a higher initial contrail ice crystal number, which in turn, lowers the ice crystal sizes and its sedimentation rate, thereby prolonging the contrail lifetime, and increase the magnitude and variability of $EF_{contrail}$ (Teoh et al., 2022a). Although the global mean $EF_{contrail}$ for the low nvPM group ($0.15 \times 10^8$ J m$^{-1}$) is around one order of magnitude smaller than the nominal nvPM group ($5.54 \times 10^8$ J m$^{-1}$) (Fig. 4c), we note that the $EF_{contrail}$ estimates from the low nvPM group are likely underestimated because CoCiP does not currently account for the potential activation of volatile particulate matter and ambient aerosols to form contrail ice crystals in the "soot-poor" regime (nvPM $EI_n < 10^{13}$ kg$^{-1}$) (Kärcher and Yu, 2009).

Unlike a map of the ISSR coverage area, which identifies regions prone to persistent contrail formation, the 4D $EF_{contrail}$ per flight distance estimates the expected contrail climate forcing of flying through a specific airspace. This approach enables targeted mitigation by identifying regions forecast to produce strongly warming contrails (i.e., grid cells with $EF_{contrail}$ greater than the 80$^{th}$ percentile), rather than all persistent contrails. When considering navigational contrail avoidance, this approach minimises potential disruptions to air traffic management and airspace capacity. The 2019 global annual mean percentage of airspace volumes forecasted with strongly warming contrails, i.e., 0.44% for $EF_{contrail} > 1.54 \times 10^9$ J m$^{-1}$ (95$^{th}$ percentile), 1.6% for $EF_{contrail} > 5.0 \times 10^8$ J m$^{-1}$ (80$^{th}$ percentile), and 4.8% for $EF_{contrail} > 0$ (net warming contrails), are up to 93% smaller than the ISSR coverage area (6.6%, for $EF_{contrail} \neq 0$) (Fig. 5a).

https://doi.org/10.5194/egusphere-2024-1361
Preprint. Discussion started: 20 June 2024


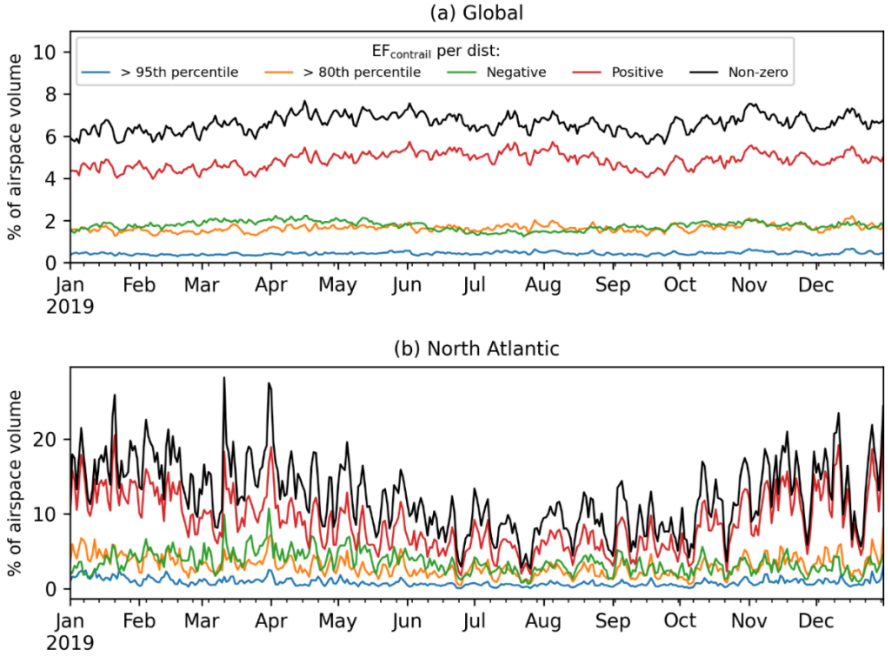


**Figure 5: Daily means of the percentage of airspace volume: (a) globally; and (b) over the North Atlantic region (between 40–63°N and 70–5°W) in 2019, where the EF$_{contrail}$ per flight distance is: (i) greater than 1.54 ×10$^{9}$ J m$^{-1}$ (95$^{th}$ percentile, blue lines); (ii) greater than 5.0 ×10$^{8}$ J m$^{-1}$ (80$^{th}$ percentile, orange lines); (iii) negative (i.e., cooling contrails, green lines); (iv) positive (i.e., warming contrails, red lines); and (v) non-zero (i.e., all contrails, black lines).**

We also use the 2019 grid-based global contrail simulation to quantify the global annual mean EF$_{contrail}$ per flight distance (Fig. 6) and annual occurrence of strongly warming (EF$_{contrail}$ > 1.54 ×10$^{9}$ J m$^{-1}$, 95$^{th}$ percentile) and cooling contrails (EF$_{contrail}$ < -2.39 ×10$^{8}$ J m$^{-1}$, 5$^{th}$ percentile) at different altitudes (Fig. 7). The grid-based CoCiP generally provides results that are consistent with prior research (Bier and Burkhardt, 2022; Gettelman et al., 2021; Teoh et al., 2022a, 2023). The absence of persistent contrails below 35,000 feet in the tropics (Fig. 6a and 6b) is primarily attributed to its higher relative ambient temperatures and tropopause height (Santer et al., 2003), while the lower relative EF$_{contrail}$ per flight distance at the subtropics (i.e., China, India, Middle East, and Australia, as shown in Fig. 6c) is associated with a lower persistent contrail formation due to the Hadley circulation (Teoh et al., 2023). Diurnal and seasonal effects contribute to a higher prevalence of both strongly warming and cooling contrails at higher latitudes due to the significant seasonal variations in daylight hours (Fig. 7a to 7d). Background radiation fields, such as the solar direct radiation (SDR), reflected solar radiation (RSR), outgoing longwave radiation (OLR) and albedo (RSR/SDR), are influenced by latitude, natural cirrus occurrence, and surface temperature and albedo. In general, regions with a higher relative albedo (e.g., poles, Siberia, and areas with high natural cirrus coverage), OLR (e.g., tropics and the Sahara Desert), and a lower relative SDR (e.g., wintertime) tend to exhibit more strongly warming contrails (Fig. 6 and 7). In contrast, regions and times with a larger relative SDR-to-OLR ratio (e.g., Southeast Asia, springtime at high latitudes) are associated with more strongly cooling contrails (Fig. 7b, 7d, and 7f). Finally, global atmospheric circulation patterns can also influence the humidity transport underlying ISSR occurrence

https://doi.org/10.5194/egusphere-2024-1361
Preprint. Discussion started: 20 June 2024


(i.e., Hadley Circulation and North Atlantic warm conveyor belt) and preferential advection of persistent contrails to specific regions (Teoh et al., 2023; Voigt et al., 2017; Wolf et al., 2024).

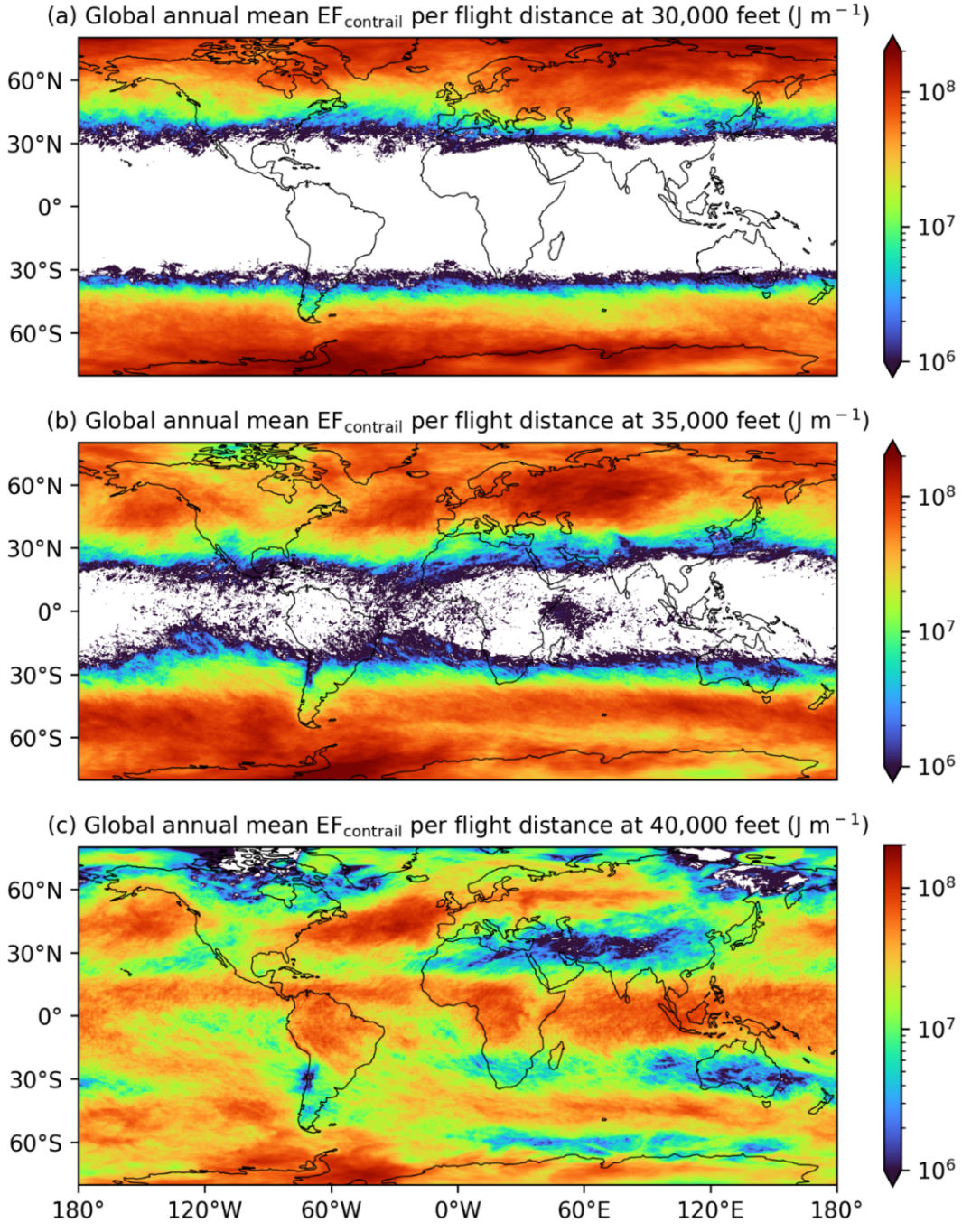


**Figure 6: The 2019 global annual mean EF$_{contrail}$ per flight distance from the grid-based CoCiP at an altitude of: (a) 30,000 feet; (b) 35,000 feet; and (c) 40,000 feet, for the nominal nvPM aircraft-engine group. Basemap plotted using Cartopy 0.22.0 and sourced from Natural Earth; licensed under public domain.**

https://doi.org/10.5194/egusphere-2024-1361
Preprint. Discussion started: 20 June 2024


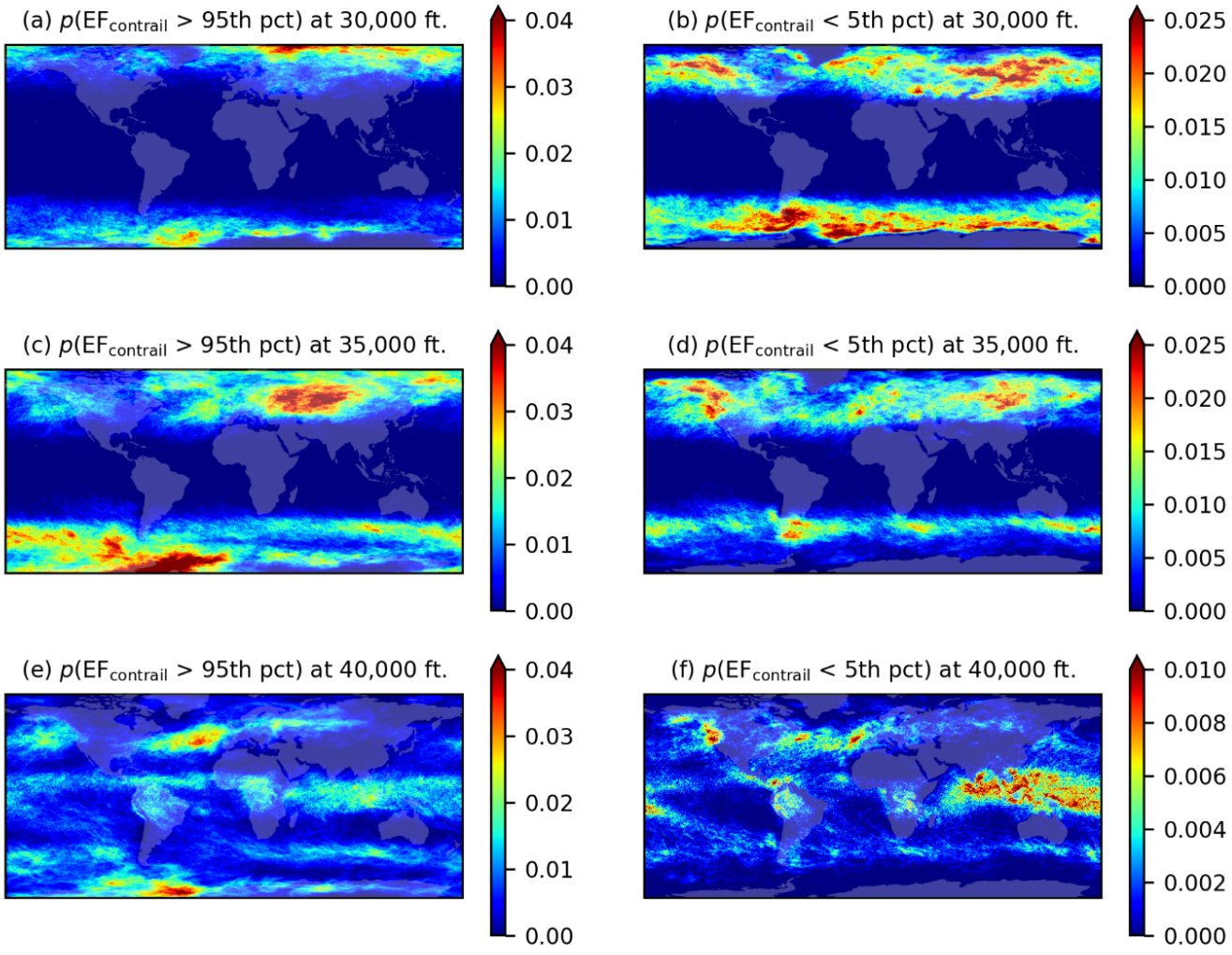


**Figure 7: The 2019 annual probability of the $EF_{contrail}$ per flight distance at each grid cell being above the 95$^{th}$ percentile (1.54 ×10$^{9}$ J m$^{-1}$) and below the 5$^{th}$ percentile (-2.39 ×10$^{8}$ J m$^{-1}$) at 30,000 feet (a, b), 35,000 feet (c, d), and 40,000 feet (e, f). Basemap plotted using Cartopy 0.22.0 and sourced from Natural Earth; licensed under public domain.**

### 5.2 Flight trajectory optimisation

The contrail climate forcing estimates from the grid-based CoCiP can be applied within the context of flight trajectory optimization. We demonstrate two possible optimization strategies using an in-house flight trajectory optimizer (described in Appendix A5) to optimize the trajectory of an actual transatlantic flight that was flown by a B77W from New York to Cairo on the 7$^{th}$ of January 2019.

https://doi.org/10.5194/egusphere-2024-1361
Preprint. Discussion started: 20 June 2024


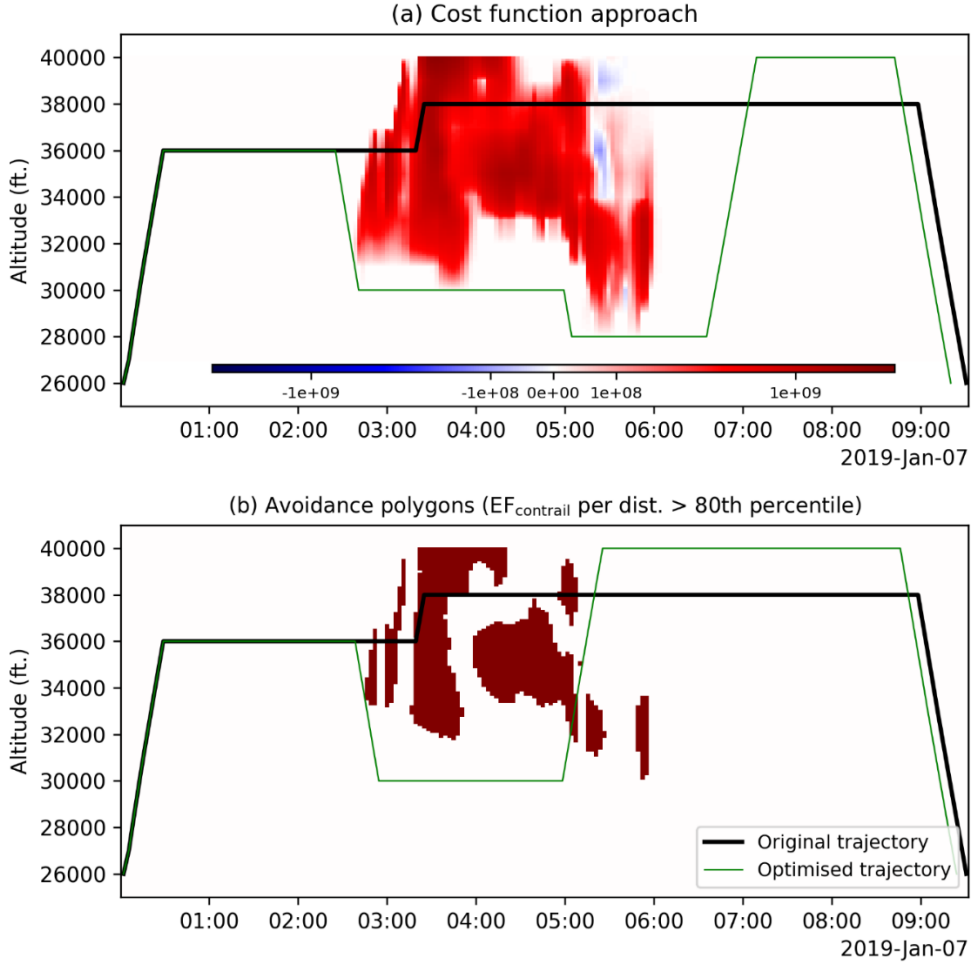


**Figure 8: Application of the grid-based CoCiP in flight trajectory optimization, where the: (a) 4D $EF_{contrail}$ per flight distance flown is integrated as an additional cost component, c.f. Eq. (8); or (b) airspace volumes that are expected to form strongly warming contrails (i.e., $EF_{contrail} > 80^{th}$ percentile ($5 \times 10^8$ J m$^{-1}$), highlighted in red, are avoided. For both optimization methods, the original and optimized flight trajectories are depicted by the black and green lines respectively, and the optimized trajectories are not checked for real-world air traffic management constraints.**

### 5.2.1 Cost-based optimisation

The 4D $EF_{contrail}$ per flight distance fields (shown in Fig. 4a) take the form of a standard weather forecast field and can be incorporated into the flight trajectory optimizer as an additional cost factor alongside existing cost parameters such as the fuel consumption and overflight charges (Martin Frias et al., 2024). To do so, flight planners can convert the $EF_{contrail}$ to a $CO_2$ mass-equivalent ($m_{CO_2,eq}$) (Teoh et al., 2023),

$$m_{CO_2,eq}\ [\text{kg}] = \frac{\text{EF}_{\text{contrail}} \times (\frac{\text{ERF}}{\text{RF}})}{\text{AGWP}_{CO_2,TH} \times S_{\text{Earth}}}, \quad (8)$$

https://doi.org/10.5194/egusphere-2024-1361
Preprint. Discussion started: 20 June 2024


where the ERF/RF ratio of 0.42 (Lee et al., 2021) is applied as a best-estimate value to convert the RF to an ERF estimate. $AGWP_{CO_2,TH}$ is the $CO_2$ absolute global warming potential over a selected time horizon (TH) ($7.54 \times 10^{-7}$ J m$^{-2}$ per kg-$CO_2$ for 20 years, or $2.78 \times 10^{-6}$ J m$^{-2}$ per kg-$CO_2$ for 100 years) (Gaillot et al., 2023), and $S_{Earth}$ is the Earth surface area ($5.101 \times 10^{14}$ m$^2$). If necessary, the $m_{CO_2,eq}$ can be further converted to a monetary value by multiplying it with the social cost of carbon ($SC_{CO_2}$), which is around US$185 [US$ 44 – 413, 5–95% range] per tonne of $CO_2$ (Rennert et al., 2022). Here, we apply Eq. (8) in the flight trajectory optimizer to minimise the total $CO_2$ emissions ($m_{CO_2,total} = m_{CO_2,fuel} + m_{CO_2,eq}$) and assume a 100-year time horizon for the $CO_2$ AGWP. We note that this is only one example of cost function, and that many other metrics are possible. The task of defining an appropriate cost function to assess trade-offs between contrail and $CO_2$ climate forcing remains a critically important topic for future research.

Using this cost-based approach, the flight trajectory optimizer successfully lowered the $m_{CO_2,total}$ by 64%, from 597,198 kg (203,285 kg of $CO_2$ emitted from the total fuel consumed + 393,913 kg from contrails) in the original trajectory to 213,357 kg (213,357 kg + 0.03 kg) in the optimized trajectory. In simpler terms, more than 99.9% of the total $EF_{contrail}$ ($1.33 \times 10^{15}$ J in the original trajectory vs. $1.04 \times 10^{8}$ J in the optimized trajectory) is mitigated at the expense of a 4.7% increase in total fuel consumption. This is achieved by: (i) lowering the cruise altitude from 36,000 to 30,000 feet between 02:45 and 05:00 UTC; followed by (ii) a further descent to 28,000 feet between 05:00 UTC and 06:30 UTC to avoid regions forecasted with persistent warming contrails; and then (iii) climbing to a final cruise altitude of 40,000 feet at around 06:30 UTC to minimise the fuel consumption rate (Fig. 8a).

#### 5.2.2 Polygon-based optimisation

Alternatively, the 4D $EF_{contrail}$ per flight distance can also be used to construct contrail avoidance polygons to identify regions forecast with strongly warming contrails (Fig. 9a). These regions can be defined by when the $EF_{contrail}$ per flight distance at a grid cell exceeds a user-defined threshold, e.g., above the 80$^{th}$ percentile ($5.0 \times 10^{8}$ J m$^{-1}$) (Teoh et al., 2023). These polygons can then be integrated into existing flight planning software (Martin Frias et al., 2024), akin to weather-avoidance polygons which restrict flights from traversing in airspace volumes that are forecast with turbulence and/or thunderstorms (Rubnich and Delaura, 2010).

Using the 80$^{th}$ percentile contrail-avoidance polygons, the optimizer recommends a trajectory that reduces $m_{CO_2,total}$ by 61%, from 597,198 kg (203,285 kg of $CO_2$ emitted from the total fuel consumed + 393,913 kg from contrails) in the original trajectory to 235,782 kg (207,379 kg + 28,403 kg) in the optimized trajectory. Put differently, 93% of the total $EF_{contrail}$ ($1.33 \times 10^{15}$ J in the original trajectory vs. $9.59 \times 10^{13}$ J in the optimized trajectory) is avoided with a fuel penalty of 2.0% (Fig. 8b). This approach involves lowering the cruise altitude from 36,000 to 30,000 feet between 03:00 and 05:00 UTC, followed by a step climb to 40,000 feet at 05:00 UTC to exploit a gap in the contrail-avoidance polygon.

https://doi.org/10.5194/egusphere-2024-1361
Preprint. Discussion started: 20 June 2024


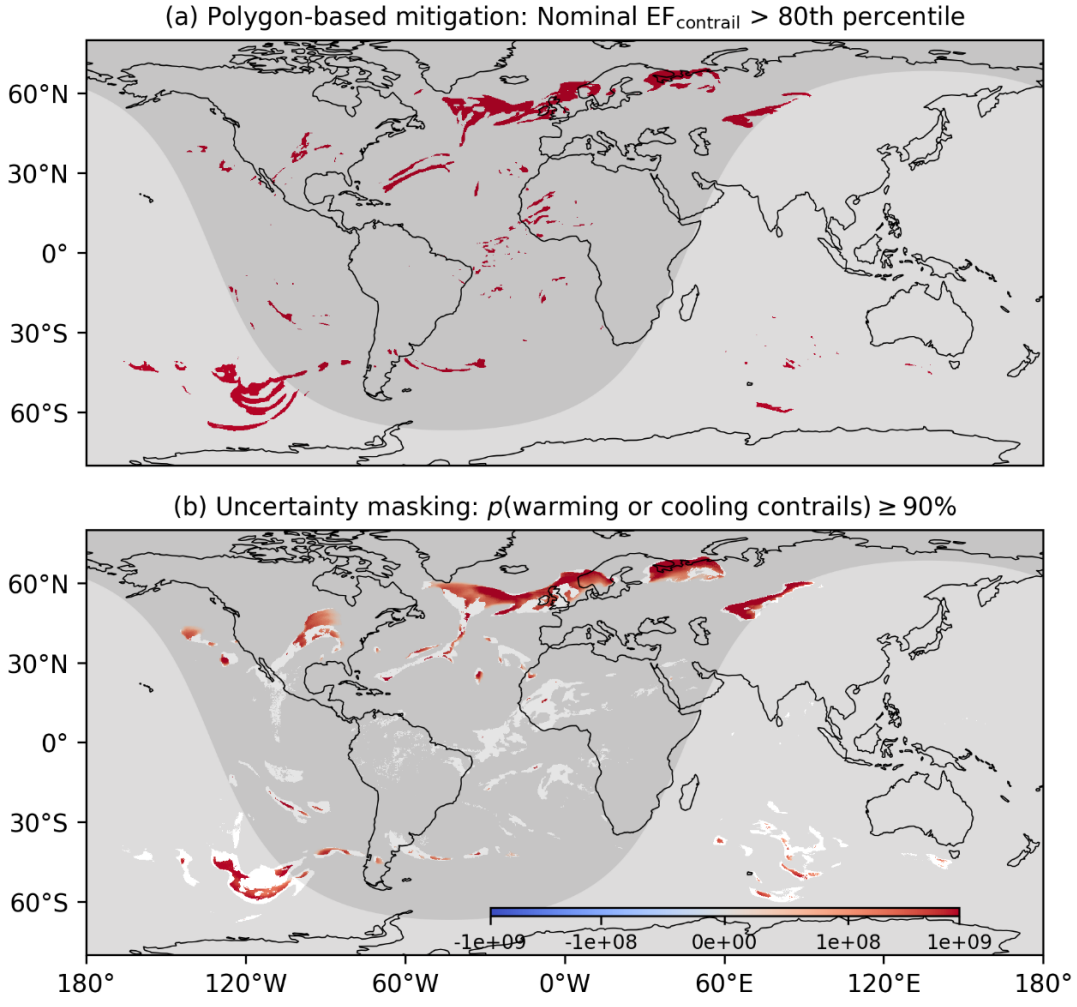


**Figure 9: Application of the simulated EF$_{contrail}$ per flight distance for contrail mitigation purposes, where flight planners can: (a) construct polygons and avoid flying in regions forecast with strongly warming contrails (i.e., grid cells where the EF$_{contrail}$ per flight distance is greater than the 80$^{th}$ percentile (5.0 ×10$^{8}$ J m$^{-1}$); and/or (b) account for uncertainties in the simulated contrail climate forcing by masking and disregarding grid cells (shown in white) when their probability of forming net warming (or cooling) contrails is less than 90%. The global contrail climate forcing shown here are from the nominal nvPM aircraft-engine group and simulated at FL360 (10,973 m) on the 7$^{th}$ of January 2019 at 03:00:00. Basemap plotted using Cartopy 0.22.0 and sourced from Natural Earth; licensed under public domain.**

### 5.3 Decision-making under uncertainty

The uncertainties in the simulated contrail climate forcing arise from various sources, such as meteorological forecasts, aircraft performance and emissions, contrail model uncertainties, and radiative transfer schemes (Platt et al., 2024). Here, we propose two strategies to incorporate these uncertainties in the decision-making process of contrail mitigation, thereby

https://doi.org/10.5194/egusphere-2024-1361
Preprint. Discussion started: 20 June 2024


increasing the probability of achieving a net climate benefit, and minimising the unintended consequences associated with increased fuel consumption and long-lived $CO_2$ emissions.

The grid-based CoCiP can be set-up to run with a Monte Carlo simulation to produce a range of $EF_{contrail}$ estimates for each grid cell (Section 3.4). This enables planners downstream to utilize a probabilistic interpretation of the $EF_{contrail}$ per flight distance to implement the cost-based or polygon-based approach (Section 5.2), while also applying an additional constraint to exclude grid cells when their probability of forming net warming contrails is less than a user-defined threshold (such as 90%, as shown in Fig. 9b). This approach aims to ensure that any mitigation action is only taken in grid cells where there is a high probability of forming net warming contrails.

Our analysis reveals three key features regarding the uncertainties in the simulated $EF_{contrail}$: (i) uncertainties in the $EF_{contrail}$ are generally largest at the edges and localised pockets of ISSRs; (ii) the sign of $EF_{contrail}$ tend to exhibit greater stability at the synoptic length scale (i.e., ISSRs with horizontal coverages of ~1000 km); and (iii) persistent contrails formed at night and in wintertime tend to exhibit lower relative uncertainty compared to those formed during daytime and in the summer (Fig. 9b). These results also suggest that contrail interventions may be more effective when implemented at a regional level rather than individual flight trajectories because the contrail uncertainties at a specific space and time may be lower than other regions.

Flight planners and policymakers could apply an additional constraint, where diversions are only applied to flights under specific circumstances, such as: (i) when there are no fuel penalties, which may be possible if the original cruise altitude and/or $V_{TAS}$ were suboptimal, or if the alternative trajectory offers more favourable wind conditions (Poll, 2017); or (ii) when the selected $CO_2$-equivalence metric from the alternative trajectory surpasses a predefined threshold of reduction relative to the original trajectory, thereby providing some margin of error to account for contrail uncertainties (Borella et al., 2024). Notably, the transition of airspace surveillance towards satellite-based systems, such as the Automatic Dependent Surveillance–Broadcast (ADS-B) standard, can improve airspace capacity and flexibility, thus increasing the likelihood of fulfilling these constraints (Molloy et al., 2022).

## 6 Conclusions

The global annual mean contrail climate forcing, which represents the largest component of aviation's overall climate forcing (Lee et al., 2021), underscores the need for heightened attention and priority from stakeholders in formulating effective mitigation solutions. As only around 2-3% of all flights are responsible for 80% of the global annual $EF_{contrail}$, one proposed solution is to re-route affected flights to avoid regions forecast with strongly warming contrails.

https://doi.org/10.5194/egusphere-2024-1361
Preprint. Discussion started: 20 June 2024


To implement this mitigation strategy in the real-world, we developed a model that forecasts regions with persistent contrails and their climate forcing. This is achieved by extending the existing trajectory-based CoCiP, which simulates contrails formed along flight trajectories, to a grid-based approach, which initializes an infinitesimal contrail segment at every point in a spatiotemporal grid and simulates the contrail climate forcing over its lifecycle. The model outputs of the grid-based CoCiP (i.e., the 5D $EF_{contrail}$ per flight distance with dimensions of longitude × latitude × altitude × time × $N$ aircraft-engine groups) are provided in a format that is consistent with standard weather and turbulence forecasts so it can be readily integrated into existing flight planning software.

Our comparison of the $EF_{contrail}$ estimates between the grid-based and trajectory-based CoCiP demonstrates a good agreement for use as a prototype contrail forecasting model (Table 4). When the grid-based CoCiP is configured with $N \geq 7$, the mean error across all performance metrics is up to 3% when compared with the configuration without any aircraft-engine grouping. Alternatively, a configuration of $N = 3$ for the grid-based CoCiP provides operational simplicity for end users, but this comes at an expense of increasing the mean error across all metrics to 13%.

Several strategies are proposed to utilize the grid-based CoCiP for contrail mitigation while accounting for uncertainties in the decision-making framework. Contrail forecasts can be integrated into flight planning software in two different ways: (i) using a cost-based approach, where the $EF_{contrail}$ is monetised and included as an additional cost component within their flight trajectory optimizer; or (ii) adopting a polygon-based approach, where "weather-avoidance" polygons are defined to avoid traversing in airspace expected to produce strongly warming contrails. The grid-based CoCiP can also be set up in a Monte Carlo formulation to estimate the probability of each grid cell forming net warming contrails ($EF_{contrail} > 0$), which in turn, enables mitigation efforts to be focused on grid cells with a high probability of forming net warming contrails (Fig. 9b). The probability of achieving a net climate benefit can also be maximised when diversions are only targeted to flights where their alternative trajectory either avoids a fuel penalty, or achieves a reduction in the user-selected $CO_2$-equivalence metric beyond a pre-defined margin of safety.

We acknowledge that the widespread adoption of our contrail forecasting model in real-world operations depends on a successful validation of its predictions against independent observations. The ongoing focus on observational validation for both CoCiP variants underscores the active efforts in this critical area. Future versions of the grid-based CoCiP are also expected to be prioritised towards: (i) accounting for contrail model uncertainties within the framework of the Monte Carlo simulation (Platt et al., 2024); (ii) incorporating contrail predictions from other models, such as Google's artificial intelligence-based predictions (Elkin and Sanekommu, 2023) and/or algorithmic climate change functions (Dietmüller et al., 2023), and only performing flight diversions in regions where there are inter-model agreements; (iii) improving the contrail forecast estimates for aircraft-engine groups that operate in the 'soot-poor' regime (nvPM $EI_n < 10^{13}$ $kg^{-1}$) by accounting for the potential activation of volatile particulate matter and ambient aerosols in forming contrail ice crystals (Kärcher et al., 2015; Kärcher and Yu, 2009); and (iv) utilising real-time observations from ground-based cameras and/or satellite images

https://doi.org/10.5194/egusphere-2024-1361
Preprint. Discussion started: 20 June 2024


(Geraedts et al., 2023; Low et al., 2024) to improve forecast accuracy and verify the outcome of any contrail mitigation actions.

## Appendix

### A1 Versioning of trajectory-based CoCiP

The original trajectory-based contrail cirrus prediction model (CoCiP), which was coded using the Fortran programming language, is versioned as "CoCiP (2012)" (Schumann, 2012; Schumann et al., 2012). Since its publication, CoCiP has undergone continuous refinement in its contrail simulation workflow and treatment of input parameters. Figure A1 provides an overview of the different versions of CoCiP and its evolution. Subsequent versions that are used by its creator Ulrich Schumann are versioned as "CoCiP-DLR" and have been extensively used in multiple studies (Jeßberger et al., 2013; Schumann et al., 2011, 2013b, a, 2015, 2021; Schumann and Graf, 2013). CoCiP-DLR incorporates additional features such as the:

- radiative heating effects on the contrail plume,
- change in contrail radiative forcing due to contrail-contrail overlapping, and
- humidity exchange between contrails and the background air.

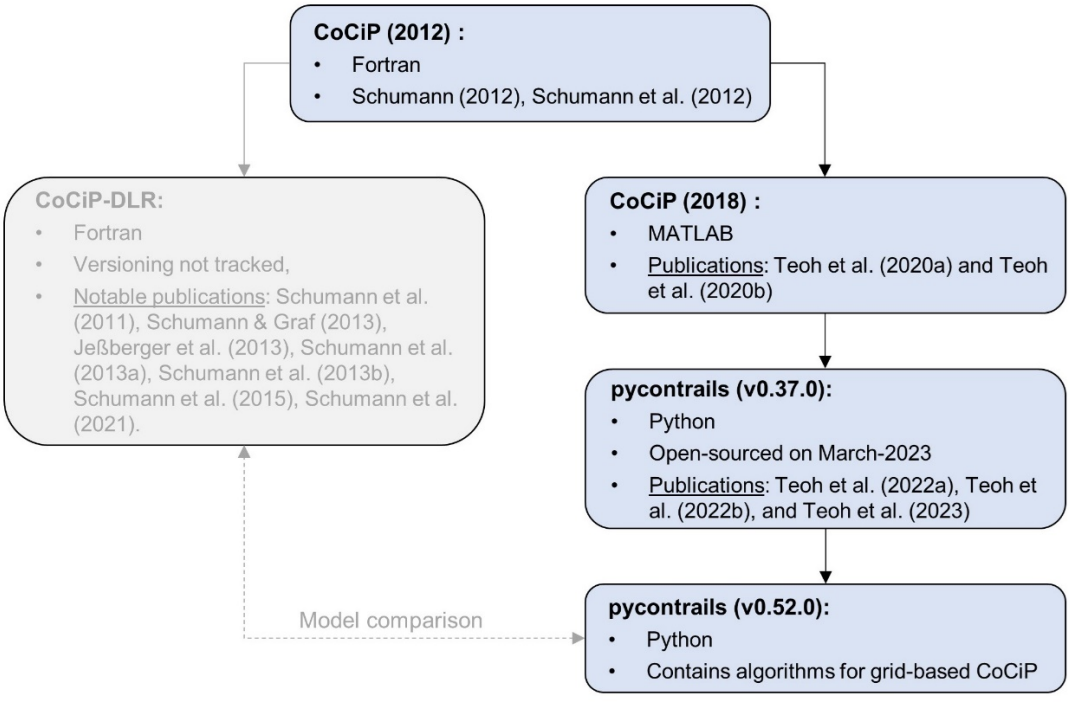


**Figure A1: Overview of the different versions of the trajectory-based CoCiP and its evolution.**

https://doi.org/10.5194/egusphere-2024-1361
Preprint. Discussion started: 20 June 2024


CoCiP (2012), which does not include the additional features from CoCiP-DLR, was forked and re-coded to MATLAB in 2018. The forked version is designated as "CoCiP (2018)". Here, we only document the changes applied from CoCiP (2018) onwards.

CoCiP (2018) has been used to two separate studies to simulate contrails over the Japanese airspace (Teoh et al., 2020b, a) with two minor improvements when compared to CoCiP (2012), including:

- The incorporation of the fractal aggregates (FA) model, which estimates the non-volatile particulate matter (nvPM) number emissions index ($EI_n$) at each flight waypoint based on the engine thrust setting and pressure ratio, rather than assuming a constant nvPM $EI_n$ ($10^{15}$ $kg^{-1}$), and
- The implementation of a Monte Carlo simulation to propagate uncertainties in the nvPM $EI_n$ estimates and meteorology to the simulated contrail properties and climate forcing.

In 2022, CoCiP (2018) was re-coded to Python and hosted on GitHub via the pycontrails repository with the goal of open sourcing it at a future date. The primary improvement in the pycontrails repository is the modularisation of various components to improve the usability of CoCiP. The different modules include flight trajectories (pycontrails.Flight), meteorology (pycontrails.MetDataset), fuel properties (pycontrails.Fuel), as well as aircraft performance and emission models (pycontrails.Model). It also features several improvements including:

- Corrections applied to the humidity fields provided by numerical weather predictions (NWP), which ensures that the provided relative humidity with respect to ice (RHi) is more consistent with in-situ measurements (Teoh et al., 2022a, 2023) (see Appendix A2),
- Utilising the $T_4/T_2$ methodology (Teoh et al., 2022a, 2024), which supersedes the FA model and estimates the aircraft-engine specific nvPM $EI_n$ using the reported nvPM emissions profile provided by the ICAO aircraft engine emissions databank (EDB) (EASA, 2021),
- Modelling the nvPM activation rate to form contrail ice crystals ($f_{activation}$), which now depends on the difference between the ambient temperature and SAC threshold temperature (Bräuer et al., 2021), which replaces the simplifying assumption that $f_{activation} = 1$ at each flight waypoint,
- Modelling the radiative heating effects on the contrail plume (Schumann et al., 2010; Schumann and Graf, 2013), and
- Simulating the change in contrail formation and properties resulting from the use of sustainable aviation fuel (SAF) (Teoh et al., 2022b).

This version is referred to as "pycontrails (v0.37.0)" and was open-sourced on March-2023 (Shapiro et al., 2023). The CoCiP model outputs from pycontrails (v0.37.0) were evaluated against those from CoCiP-DLR, revealing consistent results.

https://doi.org/10.5194/egusphere-2024-1361
Preprint. Discussion started: 20 June 2024


Since then, the pycontrails repository has been regularly updated, with the version used in this study being v0.50.2. The changes between pycontrails v0.37.0 and v0.50.2 primarily involve incorporating additional features in various modules (i.e., pycontrails.Flight, pycontrails.MetDataset), supporting the open-source Poll-Schumann (PS) aircraft performance model (Poll and Schumann, 2020, 2021, 2024), and developing algorithms related to the grid-based CoCiP. Several updates have also been applied to the trajectory-based CoCiP, including:

- Incorporating the contrail-contrail overlapping effects on the contrail radiative forcing (Schumann et al., 2021; Teoh et al., 2023),
- Addressing a typographic error in the parametric radiative forcing model in CoCiP, i.e., see Eq. (11) of Schumann et al. (2012),
- Implementing an additional humidity correction methodology, i.e., the quantile mapping approach (Wolf et al., 2023a), to ensure that the NWP-provided RHi distribution is in-line with in-situ measurements (see Appendix A2),
- Supporting additional interpolation methods across the vertical level, such as the log-log and cubic spline interpolation, to account for the non-linear lapse rate of the specific humidity, and
- Implementing a parameterized model of the ice crystal survival fraction during the wake-vortex phase, developed based on outputs from large eddy simulations (Unterstrasser, 2016).

We note that the specific changes made between pycontrails v0.37.0 and v0.51.0 are documented in detail in the change log of Shapiro et al. (2023).

**A2 Humidity correction**

Two approaches have been used in previous studies to ensure that the RHi distribution provided by the European Centre for Medium Range Weather Forecasts (ECMWF) ERA5 products are consistent with in-situ RHi measurements.

Firstly, a global humidity correction developed by Teoh et al. (2023) attempts to improve the goodness-of-fit of the ERA5-derived and in-situ RHi distribution. It scales the ERA5-derived RHi with the following parametric equations,

$$\mathrm{RHi}_{\mathrm{corrected}} = \begin{cases} \dfrac{\mathrm{RHi}}{a_{\mathrm{opt}}} & \text{for } \left(\dfrac{\mathrm{RHi}}{a_{\mathrm{opt}}}\right) \leq 1 \\ \min\left(\left(\dfrac{\mathrm{RHi}}{a_{\mathrm{opt}}}\right)^{b_{\mathrm{opt}}}, \mathrm{RHi}_{\mathrm{max}}\right) & \text{for } \left(\dfrac{\mathrm{RHi}}{a_{\mathrm{opt}}}\right) > 1 \end{cases}, \text{ where} \quad \text{(A1)}$$

$$a_{\mathrm{opt}} = \frac{a_0}{1+\exp\left(a_1 \times (|\mathrm{lat}| - a_2)\right)} + a_3\,, \quad \text{(A2)}$$

$$b_{\mathrm{opt}} = \frac{b_0}{1+\exp\left(b_1 \times (|\mathrm{lat}| - b_2)\right)} + b_3, \text{ and} \quad \text{(A3)}$$

https://doi.org/10.5194/egusphere-2024-1361
Preprint. Discussion started: 20 June 2024


$$\mathrm{RHi}_{\max} = \begin{cases} \frac{p_{\mathrm{liq}}(T_{\mathrm{amb}})}{p_{\mathrm{ice}}(T_{\mathrm{amb}})} & \text{, when } T_{\mathrm{amb}} > 235\ \mathrm{K} \\ 1.67 + (1.45 - 1.67) \times \frac{(T_{\mathrm{amb}} - 190)}{(235 - 190)} & \text{, when } T_{\mathrm{amb}} \leq 235\ \mathrm{K} \end{cases}, \quad \text{(A4)}$$

$p_{\mathrm{liq}}(T_{\mathrm{amb}})$ and $p_{\mathrm{ice}}(T_{\mathrm{amb}})$ are the saturation pressure of water vapour over liquid water and ice respectively (Sonntag, 1994). $a_{\mathrm{opt}}$ and $b_{\mathrm{opt}}$ captures the change in tropopause height between 20° and 50° N/S, which aims to account for the latitude effects on the RHi distribution. The model coefficients are re-calibrated based on the specific ERA5 product, with: (i) $a_0$ = 0.06262, $a_1$ = 0.4589, $a_2$ = 39.25, $a_3$ = 0.9522, $b_0$ = 1.471, $b_1$ = 0.04431, $b_2$ = 18.76, and $b_3$ = 1.433 for the ERA5 HRES reanalysis on pressure levels (Teoh et al., 2023); or (ii) $a_0$ = 0.02630, $a_1$ = 2.2501, $a_2$ = 36.5494, $a_3$ = 0.9651, $b_0$ = 0.4891, $b_1$ = 4.1827, $b_2$ = 17.5338, and $b_3$ = 2.2109 for the ERA5 HRES reanalysis on model levels. The main factor contributing to differences between the two set of coefficients stems from the higher vertical resolution of the ERA5 HRES on model levels relative to those on pressure levels (26 vs. 10 levels between 6,300 and 15,000 m).

Secondly, more recent studies corrected the ERA5-derived RHi using a quantile mapping approach (Platt et al., 2024; Wolf et al., 2023a). The quantile mapping approach replicates the in-situ RHi distribution by constructing two cumulative density functions (CDF) based on RHi distributions from the ERA5 and in-situ measurements, estimating the quantile value of the ERA5-derived RHi (represented on the y-axis of the CDF), and using the quantile values to substitute the ERA5-derived RHi with the in-situ RHi values.

The ERA5-corrected RHi from both methodologies (i.e., global humidity correction and quantile mapping) were compared against in-situ RHi measurements from the mid-latitude region (30°N – 70°N and 125°W – 145°E) (Hofer et al., 2024). These comparisons were conducted using the equitable threat score (ETS) metric, where an ETS = 1 suggests a perfect agreement between the ERA5-corrected and in-situ RHi, an ETS = 0 suggests a random relationship, and an ETS = -1 suggests an inverse relationship. The results show that the ETS from the quantile mapping method (0.344) is 21% higher than the global humidity correction method (0.284), and the corrected RHi from both methods represent a significant improvement relative to the uncorrected ERA5-derived RHi (0.198). However, we note that these findings are only valid for the mid-latitude region and further work is required to evaluate both the correction methodologies globally. We note that we do not prescribe for any specific humidity correction methodology, and a final decision for the operational global contrail forecasting model will be determined through stakeholder consensus. For the purposes of this paper, we employ the global humidity correction methodology instead of the quantile mapping approach because it was calibrated to account for the latitude effects, c.f. Eq. (A2) and (A3), which could be more suitable for a global contrail simulation.

https://doi.org/10.5194/egusphere-2024-1361
Preprint. Discussion started: 20 June 2024


## A3 Alternative aircraft type classifications

The grid-based CoCiP provides the simulated $EF_{contrail}$ per flight distance across five dimensions of longitude, latitude, altitude, time, and $N$ unique groups of passenger aircraft-engine types. The fifth dimension is necessary to differentiate between the contrails formed by passenger aircraft-engine types with varying nvPM number emissions and aircraft mass. Generally, a higher $N$ will improve the agreement in the simulated $EF_{contrail}$ between the trajectory-based and grid-based CoCiP, but this comes at the expense of an increase in computational resources and data storage/transfer requirements. Tables 2 and 3 in the main text classifies the most-commonly used passenger aircraft-engine types into 12 groups. Here, we propose several alternative aircraft-engine classifications with $N$ ranging between 3 and 7 (groups) to assess the trade-offs between the model performance and computational requirements.

**Table A1: Classification of the commonly used passenger aircraft-engine types into 7 unique groups based on their similarities in aircraft mass and nvPM $EI_n$.**

| Aircraft-engine classification | | nvPM $EI_n$ | | |
|---|---|---|---|---|
| | | **Low** | **Nominal** | **High** |
| **Aircraft mass** | **Light** | • A19N (LEAP-1A)<br>• A20N (LEAP-1A)<br>• A21N (LEAP-1A)<br>• B38M (LEAP-1B) | • A319 (CFM56)<br>• A320 (CFM56)<br>• A321 (CFM56)<br>• B737 (CFM56)<br>• B738 (CFM56)<br>• B739 (CFM56)<br>• B752 (RB211)<br>• B753 (RB211)<br>• B762 (CF6-80E)<br>• B763 (CF6-80E) | • A19N (Pratt & Whitney)<br>• A20N (Pratt & Whitney)<br>• A21N (Pratt & Whitney)<br>• A319 (IAE V2500)<br>• A320 (IAE V2500)<br>• A321 (IAE V2500) |
| | **Medium** | • B788 (GEnx)<br>• B789 (GEnx)<br>• B78X (GEnx)<br>• B748 (GEnx) | • A332 (Trent 700/CF6-80E)<br>• A333 (Trent 700/CF6-80E)<br>• A342 (CFM56/Trent500)<br>• A343 (CFM56/Trent500)<br>• A345 (CFM56/Trent500)<br>• A346 (CFM56/Trent500)<br>• A359 (Trent XWB)<br>• A35K (Trent XWB)<br>• B788 (Trent 1000)<br>• B789 (Trent 1000)<br>• B78X (Trent 1000) | N/A |
| | **Heavy** | • B772 (GE90)<br>• B773 (GE90)<br>• B77L (GE90)<br>• B77W (GE90) | N/A | N/A |
| | **Super heavy** | N/A | • A388 (Trent 900)<br>• B742 (CF6-80C)<br>• B743 (CF6-80C)<br>• B744 (CF6-80C) | N/A |

https://doi.org/10.5194/egusphere-2024-1361
Preprint. Discussion started: 20 June 2024


**Table A2: Classification of the commonly used passenger aircraft-engine types into 6 unique groups based on their similarities in aircraft mass and nvPM $EI_n$.**

| Aircraft-engine classification | | nvPM $EI_n$ | | |
|---|---|---|---|---|
| | | **Low** | **Nominal** | **High** |
| **Aircraft mass** | **Light** | • A19N (LEAP-1A)<br>• A20N (LEAP-1A)<br>• A21N (LEAP-1A)<br>• B38M (LEAP-1B) | • A319 (CFM56)<br>• A320 (CFM56)<br>• A321 (CFM56)<br>• B737 (CFM56)<br>• B738 (CFM56)<br>• B739 (CFM56)<br>• B752 (RB211)<br>• B753 (RB211)<br>• B762 (CF6-80E)<br>• B763 (CF6-80E) | • A19N (Pratt & Whitney)<br>• A20N (Pratt & Whitney)<br>• A21N (Pratt & Whitney)<br>• A319 (IAE V2500)<br>• A320 (IAE V2500)<br>• A321 (IAE V2500) |
| | **Medium/Heavy** | • B788 (GEnx)<br>• B789 (GEnx)<br>• B78X (GEnx)<br>• B748 (GEnx) | • A332 (Trent 700/CF6-80E)<br>• A333 (Trent 700/CF6-80E)<br>• A342 (CFM56/Trent500)<br>• A343 (CFM56/Trent500)<br>• A345 (CFM56/Trent500)<br>• A346 (CFM56/Trent500)<br>• A359 (Trent XWB)<br>• A35K (Trent XWB)<br>• B772 (GE90)<br>• B773 (GE90)<br>• B77L (GE90)<br>• B77W (GE90)<br>• B788 (Trent 1000)<br>• B789 (Trent 1000)<br>• B78X (Trent 1000) | N/A |
| | **Super heavy** | N/A | • A388 (Trent 900)<br>• B742 (CF6-80C)<br>• B743 (CF6-80C)<br>• B744 (CF6-80C) | N/A |

**Table A3: Classification of the commonly used passenger aircraft-engine types into 5 unique groups based on their similarities in aircraft mass and nvPM $EI_n$.**

| Aircraft-engine classification | | nvPM $EI_n$ | | |
|---|---|---|---|---|
| | | **Low** | **Nominal** | **High** |
| **Aircraft mass** | **Light** | • A19N (LEAP-1A)<br>• A20N (LEAP-1A)<br>• A21N (LEAP-1A)<br>• B38M (LEAP-1B) | • A319 (CFM56)<br>• A320 (CFM56)<br>• A321 (CFM56)<br>• B737 (CFM56)<br>• B738 (CFM56)<br>• B739 (CFM56)<br>• B752 (RB211)<br>• B753 (RB211)<br>• B762 (CF6-80E)<br>• B763 (CF6-80E) | • A19N (Pratt & Whitney)<br>• A20N (Pratt & Whitney)<br>• A21N (Pratt & Whitney)<br>• A319 (IAE V2500)<br>• A320 (IAE V2500)<br>• A321 (IAE V2500) |
| | **Medium/Heavy** | • B788 (GEnx)<br>• B789 (GEnx)<br>• B78X (GEnx)<br>• B748 (GEnx) | • A332 (Trent 700/CF6-80E)<br>• A333 (Trent 700/CF6-80E)<br>• A342 (CFM56/Trent500)<br>• A343 (CFM56/Trent500)<br>• A345 (CFM56/Trent500)<br>• A346 (CFM56/Trent500)<br>• A359 (Trent XWB)<br>• A35K (Trent XWB)<br>• A388 (Trent 900)<br>• B742 (CF6-80C)<br>• B743 (CF6-80C) | N/A |

https://doi.org/10.5194/egusphere-2024-1361
Preprint. Discussion started: 20 June 2024


| | | | | |
|---|---|---|---|---|
| | | | • B744 (CF6-80C)<br>• B772 (GE90)<br>• B773 (GE90)<br>• B77L (GE90)<br>• B77W (GE90)<br>• B788 (Trent 1000)<br>• B789 (Trent 1000)<br>• B78X (Trent 1000) | |

**Table A4: Classification of the commonly used passenger aircraft-engine types into 4 unique groups based on their similarities in aircraft mass and nvPM $EI_n$.**

| Aircraft-engine classification | | nvPM $EI_n$ | | |
|---|---|---|---|---|
| | | Low | Nominal/High | |
| Aircraft mass | Light | • A19N (LEAP-1A)<br>• A20N (LEAP-1A)<br>• A21N (LEAP-1A)<br>• B38M (LEAP-1B) | • A19N (Pratt & Whitney)<br>• A20N (Pratt & Whitney)<br>• A21N (Pratt & Whitney)<br>• A319 (CFM56)<br>• A319 (IAE V2500)<br>• A320 (CFM56)<br>• A320 (IAE V2500)<br>• A321 (CFM56) | • A321 (IAE V2500)<br>• B737 (CFM56)<br>• B738 (CFM56)<br>• B739 (CFM56)<br>• B752 (RB211)<br>• B753 (RB211)<br>• B762 (CF6-80E)<br>• B763 (CF6-80E) |
| | Medium/Heavy | • B788 (GEnx)<br>• B789 (GEnx)<br>• B78X (GEnx)<br>• B748 (GEnx) | • A332 (Trent 700/CF6-80E)<br>• A333 (Trent 700/CF6-80E)<br>• A342 (CFM56/Trent500)<br>• A343 (CFM56/Trent500)<br>• A345 (CFM56/Trent500)<br>• A346 (CFM56/Trent500)<br>• A359 (Trent XWB)<br>• A35K (Trent XWB)<br>• A388 (Trent 900)<br>• B742 (CF6-80C) | • B743 (CF6-80C)<br>• B744 (CF6-80C)<br>• B772 (GE90)<br>• B773 (GE90)<br>• B77L (GE90)<br>• B77W (GE90)<br>• B788 (Trent 1000)<br>• B789 (Trent 1000)<br>• B78X (Trent 1000) |

**Table A5: Classification of the commonly used passenger aircraft-engine types into 3 unique groups based on their similarities in nvPM $EI_n$.**

| Aircraft-engine classification | | | | |
|---|---|---|---|---|
| nvPM $EI_n$ | Low | • A19N (LEAP-1A)<br>• A20N (LEAP-1A)<br>• A21N (LEAP-1A) | • B38M (LEAP-1B)<br>• B788 (GEnx)<br>• B789 (GEnx) | • B78X (GEnx)<br>• B748 (GEnx) |
| | Nominal | • A319 (CFM56)<br>• A320 (CFM56)<br>• A321 (CFM56)<br>• B737 (CFM56)<br>• B738 (CFM56)<br>• B739 (CFM56)<br>• B752 (RB211)<br>• B753 (RB211)<br>• B762 (CF6-80E)<br>• B763 (CF6-80E) | • A332 (Trent 700/CF6-80E)<br>• A333 (Trent 700/CF6-80E)<br>• A342 (CFM56/Trent500)<br>• A343 (CFM56/Trent500)<br>• A345 (CFM56/Trent500)<br>• A346 (CFM56/Trent500)<br>• A359 (Trent XWB)<br>• A35K (Trent XWB)<br>• B772 (GE90)<br>• B773 (GE90) | • B77L (GE90)<br>• B77W (GE90)<br>• B788 (Trent 1000)<br>• B789 (Trent 1000)<br>• B78X (Trent 1000)<br>• A388 (Trent 900)<br>• B742 (CF6-80C)<br>• B743 (CF6-80C)<br>• B744 (CF6-80C) |
| | High | • A19N (Pratt & Whitney)<br>• A20N (Pratt & Whitney)<br>• A21N (Pratt & Whitney)<br>• A319 (IAE V2500)<br>• A320 (IAE V2500)<br>• A321 (IAE V2500) | • A319 (IAE V2500)<br>• A320 (IAE V2500)<br>• A321 (IAE V2500) | |

https://doi.org/10.5194/egusphere-2024-1361
Preprint. Discussion started: 20 June 2024


### A4 Comparison metrics

Section 4 in the main text assessed the agreement in the simulated contrail climate forcing between the trajectory-based ($EF^{traj}_{contrail}$) and grid-based CoCiP ($EF^{grid}_{contrail}$) using four different approaches: (i) the false negative and false alarm rate; (ii) the modified mean absolute log error (modified-MALE); (iii) the weighted Kendall rank correlation coefficient ($\tau_w$); and (iv) two custom performance curves (Platt et al., 2024) which evaluates the effectiveness of contrail mitigation when interventions are based on an imperfect prediction of the $EF_{contrail}$. Approaches (i) and (ii) evaluates the point-wise errors between $EF^{traj}_{contrail}$ and $EF^{grid}_{contrail}$ at each contrail segment, while approaches (iii) and (iv) assesses the model agreement at the fleet-aggregated level. Here, we provide a detailed description of approaches (ii), (iii), and (iv) and discuss the rationale behind their inclusion.

Firstly, the modified-MALE describes the relative errors in the magnitude of $EF_{contrail}$ at each flight segment, and is calculated based on the actual ($F_{true}$) and predicted ($F_{predicted}$) $EF_{contrail}$,

$$\text{MALE} = \frac{\sum_{i=1}^{i=N} |L_{\text{true},i} - L_{\text{pred},i}|}{N}, \text{ where} \quad \text{(A5)}$$

$$L_{x,i} = \text{sgn}(F_{x,i}) \times \max\left(\log\left(\frac{1+|F_{x,i}|}{|F_{\text{min}}|}\right), 0\right). \quad \text{(A6)}$$

$N$ represents the total number of data points in the sample, the subscript $x$ denotes the true or predicted $EF_{contrail}$, $\text{sgn}(F_{x,i})$ is the sign of $F_{x,I}$ (1 or -1), and $F_{min}$ is set to $10^7$ J m$^{-1}$. The modified-MALE calculates the average errors between $EF^{traj}_{contrail}$ and $EF^{grid}_{contrail}$ at the flight waypoint level, with a focus on accurately predicting moderately and strongly warming and cooling contrail segments. It achieves this by minimising the impact of prediction errors in segments with a weak $EF_{contrail}$ ($< 10^7$ J m$^{-1}$). A value of 1 implies that, on average, the $EF^{grid}_{contrail}$ is off by one order of magnitude relative to $EF^{traj}_{contrail}$.

Secondly, we calculate $\tau_w$ to assess the grid-based CoCiP's accuracy in ranking flight segments according to their magnitude of $EF_{contrail}$,

$$\tau_w = \frac{\sum_{i<j} w_{ij} \times \text{sgn}(F_{\text{true,i}} - F_{\text{true,j}}) \times \text{sgn}(F_{\text{pred,i}} - F_{\text{pred,j}})}{\sum_{i<j} w_{ij}}, \text{ where} \quad \text{(A7)}$$

$$w_{ij} = F_{\text{true,i}} + F_{\text{true,j}}. \quad \text{(A8)}$$

$\tau_w$ measures the correlation between two rankings based on the proportion of concordant and discordant pairs. A $\tau_w$ value of 1 indicates a perfect match between the rankings, a value of 0 indicates an absence of association between $F_{true}$ and $F_{pred}$, while a value of -1 means that no pairs share the same ordering. For the purposes of evaluating the grid-based CoCiP, we only include flight waypoints if $F_{true} > F_{min}$ ($= 10^7$ J m$^{-1}$), and the $w_{ij}$ term is introduced to assign larger weights to correctly rank flight segments with a large $EF_{contrail}$, consistent with the approach used in the modified-MALE. The primary distinction between the modified-MALE and $\tau_w$ lies in their treatment of pointwise errors (i.e., difference in the magnitude of $EF_{contrail}$

https://doi.org/10.5194/egusphere-2024-1361
Preprint. Discussion started: 20 June 2024


between the trajectory-based and grid-based CoCiP), where $\tau_w$ disregards these errors unless they are significant enough to alter their relative rankings.

Thirdly, the two performance curves are formulated to measure the impact of model errors on the effectiveness of contrail mitigation when interventions are prioritised to specific flight segments based on an imperfect prediction of the $EF_{contrail}$ per flight distance. More specifically, the performance curves are constructed with the following steps:

1. Given the $EF^{traj}_{contrail}$ and $EF^{grid}_{contrail}$ on a common set of contrail segments (indexed from $i$ = 1 to $N$), sort the waypoint indices into two distinct lists of $p_{traj}(i)$ and $p_{grid}(i)$. More specifically, $p_{traj}(i)$ sorts the $EF^{traj}_{contrail}$ from largest to smallest and represents prioritising flight segments for mitigation based on perfect knowledge of the contrail climate forcing, while $p_{grid}(i)$ sorts the $EF^{grid}_{contrail}$ from largest to smallest and represents prioritisations based on an imperfect prediction of the contrail climate forcing.
2. Calculate four cumulative sums, $F(x)$, for the $EF_{contrail}$ and flight segment lengths ($L$) for the trajectory-based and grid-based CoCiP,

$$F\left(EF^{traj}_{contrail,k}\right) = \sum_{p_{traj}(i)=1}^{k} EF^{traj}_{contrail,i}, \quad \text{(A9)}$$

$$F(L^{traj}_{k}) = \sum_{p_{traj}(i)=1}^{k} L_i, \quad \text{(A10)}$$

$$F(EF^{grid}_{contrail,k}) = \sum_{p_{grid}(i)=1}^{k} EF^{traj}_{contrail,i}, \text{ and} \quad \text{(A11)}$$

$$F(L^{grid}_{k}) = \sum_{p_{grid}(i)=1}^{k} L_i, \quad \text{(A12)}$$

3. Construct two absolute cumulative density functions by plotting $F\left(EF^{traj}_{contrail,k}\right)$ versus $F(L^{traj}_{k})$ and $F(EF^{grid}_{contrail,k})$ versus $F(L^{grid}_{k})$, both of which represents the performance curves for the trajectory-based and grid-based CoCiP respectively.

An example of these performance curves is shown in Fig. 2 in the main text. We then use these performance curves to derive two metrics that evaluates the effectiveness of contrail mitigation based on imperfect knowledge of the $EF_{contrail}$:

- The change in initial mitigation rate, i.e., the relative reduction in $EF_{contrail}$ per unit of re-routed flight distance for the most strongly warming contrails, which is estimated as the gradient of a secant line ($m$) from the origin to the 5$^{th}$ percentile of $F\left(EF^{traj}_{contrail}\right)$ and $F\left(EF^{grid}_{contrail}\right)$ and expressed as a ratio of $\frac{m^{grid}_{k=5}}{m^{traj}_{k=5}}$, and

https://doi.org/10.5194/egusphere-2024-1361
Preprint. Discussion started: 20 June 2024


- The change in the total flight distance flown that contributes to 80% of the total $EF_{contrail}$, which is estimated as a ratio of $\frac{F(L_{k=80}^{grid})}{F(L_{k=80}^{traj})}$.

In essence, $\frac{m_{k=5}^{grid}}{m_{k=5}^{traj}} (< 1)$ quantifies the reduced effectiveness of the grid-based CoCiP in mitigating the most strongly warming contrails when compared to the trajectory-based CoCiP; while $\frac{F(L_{k=80}^{grid})}{F(L_{k=80}^{traj})} (> 1)$ measures the additional effort that is required to mitigate 80% of the total $EF_{contrail}$ when imperfect predictions are used.

## A5 Flight trajectory optimizer

In Section 5.2, we used an in-house flight trajectory optimizer together with the 4D $EF_{contrail}$ per flight distance provided by the grid-based CoCiP to minimise the total $CO_2$ emissions ($m_{CO_2,total} = m_{CO_2,fuel} + m_{CO_2,eq}$) from a historical transatlantic flight. Here, we describe the algorithm of the flight trajectory optimizer. We note that this flight trajectory optimizer is not intended to create trajectories that could be used in real-world operations, but rather as a heuristic to estimate the time and fuel costs associated with contrail mitigation, and to demonstrate the utility of the contrail forecasts in flight planning.

The optimizer attempts to make realistic trajectories by implementing two constraints: (i) restricting the aircraft cruise altitude at designated flight levels, typically in increments of 2,000 feet; and (ii) requiring that the aircraft maintains a specific flight level for a minimum duration of 90 minutes between step climbs. Constraint (i) aims to account for the established airspace structure, which typically dictates vertical separation of flights travelling in opposite directions at intervals of 1,000 feet (ICAO, 2016); while constraint (ii) attempts to capture constraints in airspace capacity and air traffic controller workload, where flights are typically not permitted to perform frequent step changes in cruise altitude (Filippone, 2015; Tobaruela, 2015). We also do not consider a full 4D flight trajectory optimization in this work. Instead, the optimization is only performed in two dimensions, namely time and altitude, while retaining the original horizontal flight path.

The main input parameter of the flight trajectory optimizer is the Cost Index (CI), which is defined as the ratio between the time and fuel related fuel costs, and the optimizer minimises the weighted objective function that combines time costs, $CO_2$ and contrail costs. The flight trajectory is divided into equal flight segments, where each segment will be traversed in approximately five minutes at a near optimal cruise speed. The search space used to find the optimal trajectory is then constrained to a 2D grid representing the flight segments (i.e., horizontal axis) and flight level (i.e., vertical axis). For the flight trajectory used in Section 5.2, the horizontal axis consisted of 207 segments, each approximately 44.8 km in length,

https://doi.org/10.5194/egusphere-2024-1361
Preprint. Discussion started: 20 June 2024


and vertical axis represents the altitude that is divided in increments of 2,000 feet between a specified minimum (assumed to be 26,000 feet) and maximum altitude (assumed to be the maximum operating altitude of the aircraft). We also ensure that the step climb/descent performed at each flight segment is realistic and does not exceed a nominal rate of climb and descent (ROCD) of 500 feet per minute.

The flight trajectory optimizer performs a breadth-first Dykstra-like search across the 2D search space. Starting from the initial point of the horizontal grid and the lowest flight level, the algorithm iterates through each of the feasible grid points to determine the optimal Mach number ($M_{\text{opt}}$) for the given aircraft type and CI. The $M_{\text{opt}}$ that minimizes the total cost of cruise at each flight segment is given by:

$$M_{\text{opt}} = \underset{M}{\text{argmin}} \left(\frac{\text{CI}+\Delta m(M)}{V_{\text{TAS}}}\right), \tag{A13}$$

where CI is the chosen cost index (assumed to be 60 in this study), $\Delta m(M)$ is the fuel burn over this flight segment for a given Mach number ($M$), and $V_{\text{TAS}}$ is the aircraft true airspeed which accounts for the ambient wind conditions. The fuel burn is computed using the Poll-Schumann (PS) aircraft performance model (Poll and Schumann, 2020, 2021, 2024) and requires the aircraft type, ambient air temperature and aircraft mass as input parameters. We then prescribe an allowed set of actions for the aircraft to proceed to the next flight segment:

- If the aircraft is at the starting point of the search, it is allowed to stay level or climb,
- If the aircraft remained level over the last horizontal segment, it must continue to remain level unless it exceeded the specified time interval (> 90 minutes) since the last altitude change,
- If the aircraft was climbing or descending over the last flight segment, the aircraft must maintain its current climb and descent until it has reached an allowed flight level for cruise, at which point it has the option to remain level or continue its climb or descent, and
- Each action will only be allowed if the required thrust and lift are within the rated operating conditions of the aircraft, as determined by the PS model.

For each allowed action, the algorithm estimates the required fuel burn to complete the action and fly to the respective grid point. At each grid point reached through an allowed action, the cumulative impact of the current flight trajectory is compared with any previously identified optimal flight path to the same grid point. Throughout each iteration, the algorithm only saves the lowest-cost path for reaching the designated grid point. The search concludes once it has examined every viable grid point, and the optimal trajectory is reconstructed by starting from the final grid point and retracing the sequence of actions that were previously taken to reach that point. We note that the optimized flight trajectories are not checked for

https://doi.org/10.5194/egusphere-2024-1361
Preprint. Discussion started: 20 June 2024


practical usage, and a real-world flight trajectory optimization needs to consider practical flight and air traffic management constraints, such as the minimum separation between aircraft, airspace congestion and design (i.e., North Atlantic Organised Track Structure), and air traffic controller workload (Molloy et al., 2022).

## Author contributions

MS and MEJS conceptualised the study. ZE, RT, TA, TD, MEJS and MS developed the methodology and undertook the investigation. ZE, RT, TA, TD and MS were responsible for software development and data curation. RT, TA and TD created or sourced the figures. RT, TA, and TD wrote the original manuscript. MS acquired funding. All authors have read, edited, and reviewed the manuscript, and agreed upon the published version of the paper.

## Model & Data availability

The `pycontrails` repository that contains the algorithms for the Poll-Schumann (PS) aircraft performance model, the trajectory-based CoCiP (`Cocip`), and the grid-based CoCiP (`CocipGrid`) is publicly available at https://doi.org/10.5281/zenodo.7776686. The grid-based CoCiP can also be accessed via an Application Programming Interface (API) at https://api.contrails.org and https://forecast.contrails.org. This document contains Copernicus Climate Change Service information from 2024. Neither the European Commission nor the ECMWF is responsible for any use of the Copernicus information.

## Competing interests

The authors declare that they have no conflict of interest.

## References

Agarwal, A., Meijer, V. R., Eastham, S. D., Speth, R. L., and Barrett, S. R. H.: Reanalysis-driven simulations may overestimate persistent contrail formation by 100-250%, Environmental Research Letters, 17, 1–14, https://doi.org/10.1088/1748-9326/AC38D9, 2022.

American Airlines: American Airlines participates in first-of-its-kind research on contrail avoidance, https://news.aa.com/news/news-details/2023/American-Airlines-participates-in-first-of-its-kind-research-on-contrail-avoidance-CORP-OTH-08/default.aspx, (last access: 8th August 2023), 2023.

https://doi.org/10.5194/egusphere-2024-1361
Preprint. Discussion started: 20 June 2024


Bier, A. and Burkhardt, U.: Impact of Parametrizing Microphysical Processes in the Jet and Vortex Phase on Contrail Cirrus Properties and Radiative Forcing, Journal of Geophysical Research: Atmospheres, 127, e2022JD036677, https://doi.org/10.1029/2022JD036677, 2022.

Borella, A., Boucher, O., Shine, K., Stettler, M. E. J., Tanaka, K., Teoh, R., and Bellouin, N.: The importance of an informed choice of CO2-equivalence metrics for contrail avoidance [Pre-print], EGUsphere, https://doi.org/https://doi.org/10.5194/egusphere-2024-347, 2024.

Bräuer, T., Voigt, C., Sauer, D., Kaufmann, S., Hahn, V., Scheibe, M., Schlager, H., Diskin, G. S., Nowak, J. B., DiGangi, J. P., Huber, F., Moore, R. H., and Anderson, B. E.: Airborne Measurements of Contrail Ice Properties—Dependence on Temperature and Humidity, Geophys Res Lett, 48, e2020GL092166, https://doi.org/10.1029/2020GL092166, 2021.

Caiazzo, F., Agarwal, A., Speth, R. L., and Barrett, S. R. H.: Impact of biofuels on contrail warming, Environmental Research Letters, 12, 114013, https://doi.org/https://doi.org/10.1088/1748-9326/aa893b, 2017.

Chen, C. C. and Gettelman, A.: Simulated radiative forcing from contrails and contrail cirrus, Atmos Chem Phys, 13, 12525–12536, https://doi.org/10.5194/acp-13-12525-2013, 2013.

Dietmüller, S., Matthes, S., Dahlmann, K., Yamashita, H., Simorgh, A., Soler, M., Linke, F., Lührs, B., Meuser, M. M., Weder, C., Grewe, V., Yin, F., and Castino, F.: A Python library for computing individual and merged non-CO $_2$ algorithmic climate change functions: CLIMaCCF V1.0, Geosci Model Dev, 16, 4405–4425, https://doi.org/10.5194/GMD-16-4405-2023, 2023.

Duda, D. P., Bedka, S. T., Minnis, P., Spangenberg, D., Khlopenkov, K., Chee, T., and Smith, W. L.: Northern Hemisphere contrail properties derived from Terra and Aqua MODIS data for 2006 and 2012, Atmos Chem Phys, 19, 5313–5330, https://doi.org/10.5194/ACP-19-5313-2019, 2019.

EASA: ICAO Aircraft Engine Emissions Databank (07/2021), EASA [data set], https://www.easa.europa.eu/domains/environment/icao-aircraft-engine-emissions-databank (last access: 15 February 2022), 2021.

ECMWF: Atmospheric Model high resolution 10-day forecast (Set I - HRES), ECMWF [data set] https://www.ecmwf.int/en/forecasts/datasets/set-i (last access: 12 April 2024), 2024.

Edwards, H. A., Dixon-Hardy, D., and Wadud, Z.: Aircraft cost index and the future of carbon emissions from air travel, Appl Energy, 164, 553–562, https://doi.org/10.1016/J.APENERGY.2015.11.058, 2016.

https://doi.org/10.5194/egusphere-2024-1361
Preprint. Discussion started: 20 June 2024


Elkin, C. and Sanekommu, D.: How AI is helping airlines mitigate the climate impact of contrails, Google, https://blog.google/technology/ai/ai-airlines-contrails-climate-change/ (last access: 12 March 2024), 2023.

European Commission: Directive (EU) 2023/958 of the European Parliament and of the Council of 10 May 2023, European Commission, https://eur-lex.europa.eu/legal-content/EN/TXT/PDF/?uri=CELEX:32023L0958 (last access: 6 May 2024), 2023.

Filippone, A.: Assessment of aircraft contrail avoidance strategies, J Aircr, 52, 872–877, https://doi.org/10.2514/1.C033176, 2015.

Fritz, T. M., Eastham, S. D., Speth, R. L., and Barrett, S. R. H.: The role of plume-scale processes in long-term impacts of aircraft emissions, Atmos Chem Phys, 20, 5697–5727, https://doi.org/10.5194/ACP-20-5697-2020, 2020.

Gaillot, T., Beauchet, S., Lorne, D., and Krim, L.: The impact of fossil jet fuel emissions at altitude on climate change: A life cycle assessment study of a long-haul flight at different time horizons, Atmos Environ, 311, 119983, https://doi.org/10.1016/J.ATMOSENV.2023.119983, 2023.

Geraedts, S., Brand, E., Dean, T. R., Eastham, S., Elkin, C., Engberg, Z., Hager, U., Langmore, I., McCloskey, K., Ng, J. Y.-H., Platt, J. C., Sankar, T., Sarna, A., Shapiro, M., and Goyal, N.: A scalable system to measure contrail formation on a per-flight basis, https://arxiv.org/abs/2308.02707v6, 2023.

Gettelman, A., Chen, C. C., and Bardeen, C. G.: The climate impact of COVID-19-induced contrail changes, Atmos Chem Phys, 21, 9405–9416, https://doi.org/10.5194/ACP-21-9405-2021, 2021.

Gierens, K., Matthes, S., and Rohs, S.: How Well Can Persistent Contrails Be Predicted?, Aerospace, 7, 169, https://doi.org/10.3390/AEROSPACE7120169, 2020.

Haywood, J. M., Allan, R. P., Bornemann, J., Forster, P. M., Francis, P. N., Milton, S., Rädel, G., Rap, A., Shine, K. P., and Thorpe, R.: A case study of the radiative forcing of persistent contrails evolving into contrail-induced cirrus, Journal of Geophysical Research: Atmospheres, 114, D24201, https://doi.org/10.1029/2009JD012650, 2009.

Hersbach, H., Bell, B., Berrisford, P., Hirahara, S., Horányi, A., Muñoz-Sabater, J., Nicolas, J., Peubey, C., Radu, R., Schepers, D., Simmons, A., Soci, C., Abdalla, S., Abellan, X., Balsamo, G., Bechtold, P., Biavati, G., Bidlot, J., Bonavita, M., De Chiara, G., Dahlgren, P., Dee, D., Diamantakis, M., Dragani, R., Flemming, J., Forbes, R., Fuentes, M., Geer, A., Haimberger, L., Healy, S., Hogan, R. J., Hólm, E., Janisková, M., Keeley, S., Laloyaux, P., Lopez, P., Lupu, C., Radnoti, G., de Rosnay, P., Rozum, I., Vamborg, F., Villaume, S., and Thépaut, J. N.: The ERA5 global reanalysis, Quarterly Journal of the Royal Meteorological Society, 146, 1999–2049, https://doi.org/10.1002/qj.3803, 2020.

https://doi.org/10.5194/egusphere-2024-1361
Preprint. Discussion started: 20 June 2024


Hofer, S. M., Gierens, K., and Rohs, S.: How well can persistent contrails be predicted? - An update [pre-print], EGUsphere, https://doi.org/https://doi.org/10.5194/egusphere-2024-385, 2024.

Holzapfel, F.: Probabilistic Two-Phase Wake Vortex Decay and Transport Model, J Aircr, 40, 323–331, https://doi.org/10.2514/2.3096, 2003.

ICAO: Air Traffic Management - Procedures for Air Navigation Services, International Civil Aviation Organisation, http://flightservicebureau.org/wp-content/uploads/2017/03/ICAO-Doc4444-Pans-Atm-16thEdition-2016-OPSGROUP.pdf (last access: 6 May 2024), Montreal, Canada, 2016.

Jeßberger, P., Voigt, C., Schumann, U., Sölch, I., Schlager, H., Kaufmann, S., Petzold, A., Schäuble, D., and Gayet, J.-F.: Aircraft type influence on contrail properties, Atmos Chem Phys, 13, 11965–11984, https://doi.org/10.5194/acp-13-11965-2013, 2013.

Kärcher, B.: Formation and radiative forcing of contrail cirrus, Nat Commun, 9, 1824, https://doi.org/10.1038/s41467-018-04068-0, 2018.

Kärcher, B. and Yu, F.: Role of aircraft soot emissions in contrail formation, Geophys Res Lett, 36, L01804, https://doi.org/10.1029/2008GL036649, 2009.

Kärcher, B., Burkhardt, U., Bier, A., Bock, L., and Ford, I. J.: The microphysical pathway to contrail formation, Journal of Geophysical Research: Atmospheres, 120, 7893–7927, https://doi.org/10.1002/2015JD023491, 2015.

Lee, D. S., Fahey, D. W., Skowron, A., Allen, M. R., Burkhardt, U., Chen, Q., Doherty, S. J., Freeman, S., Forster, P. M., Fuglestvedt, J., Gettelman, A., De León, R. R., Lim, L. L., Lund, M. T., Millar, R. J., Owen, B., Penner, J. E., Pitari, G., Prather, M. J., Sausen, R., and Wilcox, L. J.: The contribution of global aviation to anthropogenic climate forcing for 2000 to 2018, Atmos Environ, 244, 117834, https://doi.org/10.1016/J.ATMOSENV.2020.117834, 2021.

Lewellen, D. C.: Persistent contrails and contrail cirrus. Part II: Full lifetime behavior, J Atmos Sci, 71, 4420–4438, https://doi.org/10.1175/JAS-D-13-0317.1, 2014.

Lewellen, D. C., Meza, O., Huebsch, W. W., Lewellen, D. C., Meza, O., and Huebsch, W. W.: Persistent Contrails and Contrail Cirrus. Part I: Large-Eddy Simulations from Inception to Demise, J Atmos Sci, 71, 4399–4419, https://doi.org/10.1175/JAS-D-13-0316.1, 2014.

Lokman, N.: MUAC Contrail Prevention Trial 2021, https://nari.arc.nasa.gov/sites/default/files/attachments/NielsLokman_Contrail PDF Slides.pdf (last access: 6 May 2024), 2022.

https://doi.org/10.5194/egusphere-2024-1361
Preprint. Discussion started: 20 June 2024


Lovegren, J. A. and Hansman, R. J.: Estimation of Potential Aircraft Fuel Burn Reduction in Cruise Via Speed and Altitude Optimization Strategies, https://dspace.mit.edu/handle/1721.1/62196, 2011.

Low, J., Teoh, R., Ponsonby, J., Gryspeerdt, E., Shapiro, M., and Stettler, M. E. J.: Ground-based contrail observations: comparisons with flight telemetry and contrail model estimates [Submitted], 2024.

Mannstein, H., Brömser, A., and Bugliaro, L.: Ground-based observations for the validation of contrails and cirrus detection in satellite imagery, Atmos Meas Tech, 3, 655–669, https://doi.org/10.5194/amt-3-655-2010, 2010.

Martin Frias, A., Shapiro, M., Engberg, Z., Zopp, R., Soler, M., and Stettler, M. E. J.: Feasibility of contrail avoidance in a commercial flight planning system: an operational analysis, Environmental Research: Infrastructure and Sustainability, 4, https://doi.org/10.1088/2634-4505/ad310c, 2024.

Meerkötter, R., Schumann, U., Doelling, D. R., Minnis, P., Nakajima, T., and Tsushima, Y.: Radiative forcing by contrails, Ann Geophys, 17, 1080–1094, https://doi.org/10.1007/s00585-999-1080-7, 1999.

Molloy, J., Teoh, R., Harty, S., Koudis, G., Schumann, U., Poll, I., and Stettler, M. E. J.: Design Principles for a Contrail-Minimizing Trial in the North Atlantic, Aerospace, 9, 375, https://doi.org/10.3390/AEROSPACE9070375, 2022.

Platt, J., Shapiro, M., Engberg, Z., Stettler, M. E. J., Teoh, R., Brand, E., McCloskey, K., Rothenburg, J., Schumann, U., and Van Arsdale, C.: Predicting highly-forcing contrails despite weather and model uncertainty [Submitted], 2024.

Poll, D. I. A.: 21st-Century civil aviation: Is it on course or is it over-confident and complacent? – thoughts on the conundrum of aviation and the environment, The Aeronautical Journal, 121, 115–140, https://doi.org/10.1017/aer.2016.140, 2017.

Poll, D. I. A. and Schumann, U.: An estimation method for the fuel burn and other performance characteristics of civil transport aircraft in the cruise. Part 1 fundamental quantities and governing relations for a general atmosphere, The Aeronautical Journal, 1–39, https://doi.org/10.1017/aer.2020.62, 2020.

Poll, D. I. A. and Schumann, U.: An estimation method for the fuel burn and other performance characteristics of civil transport aircraft during cruise: part 2, determining the aircraft's characteristic parameters, The Aeronautical Journal, 125, 296–340, https://doi.org/10.1017/AER.2020.124, 2021.

Poll, D. I. A. and Schumann, U.: On the conditions for absolute minimum fuel burn for turbofan powered, civil transport aircraft and a simple model for wave drag, The Aeronautical Journal, 1–33, https://doi.org/10.1017/AER.2024.10, 2024.

https://doi.org/10.5194/egusphere-2024-1361
Preprint. Discussion started: 20 June 2024


Ponater, M., Bickel, M., Bock, L., and Burkhardt, U.: Towards Determining the Contrail Cirrus Efficacy, Aerospace, 8, 42, https://doi.org/10.3390/AEROSPACE8020042, 2021.

Rennert, K., Errickson, F., Prest, B. C., Rennels, L., Newell, R. G., Pizer, W., Kingdon, C., Wingenroth, J., Cooke, R., Parthum, B., Smith, D., Cromar, K., Diaz, D., Moore, F. C., Müller, U. K., Plevin, R. J., Raftery, A. E., Ševčíková, H., Sheets, H., Stock, J. H., Tan, T., Watson, M., Wong, T. E., and Anthoff, D.: Comprehensive evidence implies a higher social cost of CO2, Nature 2022 610:7933, 610, 687–692, https://doi.org/10.1038/s41586-022-05224-9, 2022.

Rosenow, J., Hospodka, J., Lán, S., and Fricke, H.: Validation of a Contrail Life-Cycle Model in Central Europe, Sustainability 2023, Vol. 15, Page 8669, 15, 8669, https://doi.org/10.3390/SU15118669, 2023.

Rubnich, M. and Delaura, R.: An algorithm to identify robust convective weather avoidance polygons in en route airspace, 10th AIAA Aviation Technology, Integration and Operations Conference 2010, ATIO 2010, 2, https://doi.org/10.2514/6.2010-9164, 2010.

Santer, B. D., Sausen, R., Wigley, T. M. L., Boyle, J. S., AchutaRao, K., Doutriaux, C., Hansen, J. E., Meehl, G. A., Roeckner, E., Ruedy, R., Schmidt, G., and Taylor, K. E.: Behavior of tropopause height and atmospheric temperature in models, reanalyses, and observations: Decadal changes, Journal of Geophysical Research: Atmospheres, 108, ACL 1-1, https://doi.org/10.1029/2002JD002258, 2003.

Schumann, U.: On conditions for contrail formation from aircraft exhausts, Meteorologische Zeitschrift, 5, 4–23, https://doi.org/10.1127/metz/5/1996/4, 1996.

Schumann, U.: A contrail cirrus prediction model, Geosci Model Dev, 5, 543–580, https://doi.org/10.5194/gmd-5-543-2012, 2012.

Schumann, U. and Graf, K.: Aviation-induced cirrus and radiation changes at diurnal timescales, Journal of Geophysical Research: Atmospheres, 118, 2404–2421, https://doi.org/10.1002/jgrd.50184, 2013.

Schumann, U. and Heymsfield, A. J.: On the lifecycle of individual contrails and contrail cirrus, Meteorological Monographs, 58, 3.1-3.24, https://doi.org/10.1175/amsmonographs-d-16-0005.1, 2017.

Schumann, U., Mayer, B., Hamann, U., Graf, K.: Radiative heating in contrail cirrus, Geophysical Research Abstracts, 12 (EGU201), pp. 1-2, European Geophysical Union General Assembly 2010, 2010-05-02 – 2010-05-7, Wien, https://elib.dlr.de/67811/, 2010. Last access: 5 December 2022.

Schumann, U., Graf, K., and Mannstein, H.: Potential to reduce the climate impact of aviation by flight level changes, in: 3rd AIAA Atmospheric Space Environments Conference, https://doi.org/10.2514/6.2011-3376, 2011.

https://doi.org/10.5194/egusphere-2024-1361
Preprint. Discussion started: 20 June 2024


Schumann, U., Mayer, B., Graf, K., and Mannstein, H.: A parametric radiative forcing model for contrail cirrus, J Appl Meteorol Climatol, 51, 1391–1406, https://doi.org/10.1175/JAMC-D-11-0242.1, 2012.

Schumann, U., Jeßberger, P., and Voigt, C.: Contrail ice particles in aircraft wakes and their climatic importance, Geophys Res Lett, 40, 2867–2872, https://doi.org/10.1002/grl.50539, 2013a.

Schumann, U., Hempel, R., Flentje, H., Garhammer, M., Graf, K., Kox, S., Lösslein, H., and Mayer, B.: Contrail study with ground-based cameras, Atmos Meas Tech, 6, 3597–3612, https://doi.org/10.5194/amt-6-3597-2013, 2013b.

Schumann, U., Penner, J. E., Chen, Y., Zhou, C., and Graf, K.: Dehydration effects from contrails in a coupled contrail–climate model, Atmos Chem Phys, 15, 11179–11199, https://doi.org/10.5194/acp-15-11179-2015, 2015.

Schumann, U., Baumann, R., Baumgardner, D., Bedka, S., Duda, D., Freudenthaler, V., Gayet, J.-F., Heymsfield, A. J., Minnis, P., and Quante, M.: Properties of individual contrails: A compilation of observations and some comparisons, Atmos Chem Phys, 17, 1–62, https://doi.org/10.5194/acp-17-403-2017., 2017.

Schumann, U., Poll, I., Teoh, R., Koelle, R., Spinielli, E., Molloy, J., Koudis, G. S., Baumann, R., Bugliaro, L., Stettler, M., and Voigt, C.: Air traffic and contrail changes over Europe during COVID-19: A model study, Atmos Chem Phys, 21, 7429–7450, https://doi.org/10.5194/ACP-21-7429-2021, 2021.

Shapiro, M., Engberg, Z., Teoh, R., and Dean, T.: pycontrails: Python library for modeling aviation climate impacts, Zenodo, https://doi.org/10.5281/zenodo.7776686, 2023.

Sonntag, D.: Advancements in the field of hygrometry, Meteorologische Zeitschrift, 3, 51–66, https://doi.org/10.1127/metz/3/1994/51, 1994.

Teoh, R., Schumann, U., and Stettler, M. E. J.: Beyond Contrail Avoidance: Efficacy of Flight Altitude Changes to Minimise Contrail Climate Forcing, Aerospace, 7, 121, https://doi.org/10.3390/aerospace7090121, 2020a.

Teoh, R., Schumann, U., Majumdar, A., and Stettler, M. E. J.: Mitigating the Climate Forcing of Aircraft Contrails by Small-Scale Diversions and Technology Adoption, Environ Sci Technol, 54, 2941–2950, https://doi.org/10.1021/acs.est.9b05608, 2020b.

Teoh, R., Schumann, U., Gryspeerdt, E., Shapiro, M., Molloy, J., Koudis, G., Voigt, C., and Stettler, M.: Aviation Contrail Climate Effects in the North Atlantic from 2016-2021., Atmos. Chem. Phys., 22, 10919–10935, https://doi.org/https://doi.org/10.5194/acp-2022-169, 2022a.

https://doi.org/10.5194/egusphere-2024-1361
Preprint. Discussion started: 20 June 2024


Teoh, R., Schumann, U., Voigt, C., Schripp, T., Shapiro, M., Engberg, Z., Molloy, J., Koudis, G., and Stettler, M. E. J.: Targeted Use of Sustainable Aviation Fuel to Maximise Climate Benefits, Environ Sci Technol, 56, 17246–17255, https://doi.org/https://doi.org/10.1021/acs.est.2c05781, 2022b.

Teoh, R., Engberg, Z., Schumann, U., Voigt, C., Shapiro, M., Rohs, S., and Stettler, M. E. J.: Global aviation contrail climate effects from 2019 to 2021 [preprint], EGUsphere, https://doi.org/https://doi.org/10.5194/egusphere-2023-1859, 2023.

Teoh, R., Engberg, Z., Shapiro, M., Dray, L., and Stettler, M. E. J.: The high-resolution Global Aviation emissions Inventory based on ADS-B (GAIA) for 2019–2021, Atmos Chem Phys, 24, 725–744, https://doi.org/10.5194/ACP-24-725-2024, 2024.

Tobaruela, G.: A Framework to assess the ability of automation to deliver capacity targets in European airspace, PhD Thesis, https://doi.org/10.25560/28150, 2015.

Turbli: Turbulence forecast for your flight, https://turbli.com/ (last access: 15 April 2024), 2024.

Unterstrasser, S.: Properties of young contrails: a parametrisation based on large-eddy simulations, Atmos Chem Phys, 16, 2059–2082, https://doi.org/10.5194/acp-16-2059-2016, 2016.

Vázquez-Navarro, M., Mannstein, H., and Kox, S.: Contrail life cycle and properties from 1 year of MSG/SEVIRI rapid-scan images, Atmos Chem Phys, 15, 8739–8749, https://doi.org/10.5194/acp-15-8739-2015, 2015.

Voigt, C., Schumann, U., Minikin, A., Abdelmonem, A., Afchine, A., Borrmann, S., Boettcher, M., Buchholz, B., Bugliaro, L., Costa, A., Curtius, J., Dollner, M., Dörnbrack, A., Dreiling, V., Ebert, V., Ehrlich, A., Fix, A., Forster, L., Frank, F., Fütterer, D., Giez, A., Graf, K., Grooß, J. U., Groß, S., Heimerl, K., Heinold, B., Hüneke, T., Järvinen, E., Jurkat, T., Kaufmann, S., Kenntner, M., Klingebiel, M., Klimach, T., Kohl, R., Krämer, M., Krisna, T. C., Luebke, A., Mayer, B., Mertes, S., Molleker, S., Petzold, A., Pfeilsticker, K., Port, M., Rapp, M., Reutter, P., Rolf, C., Rose, D., Sauer, D., Schäfler, A., Schlage, R., Schnaiter, M., Schneider, J., Spelten, N., Spichtinger, P., Stock, P., Walser, A., Weigel, R., Weinzierl, B., Wendisch, M., Werner, F., Wernli, H., Wirth, M., Zahn, A., Ziereis, H., and Zöger, M.: ML-CIRRUS: The Airborne Experiment on Natural Cirrus and Contrail Cirrus with the High-Altitude Long-Range Research Aircraft HALO, Bull Am Meteorol Soc, 98, 271–288, https://doi.org/10.1175/BAMS-D-15-00213.1, 2017.

Wilhelm, L., Gierens, K., and Rohs, S.: Weather Variability Induced Uncertainty of Contrail Radiative Forcing, Aerospace 2021, Vol. 8, Page 332, 8, 332, https://doi.org/10.3390/AEROSPACE8110332, 2021.

Wolf, K., Bellouin, N., Boucher, O., Rohs, S., and Li, Y.: Correction of temperature and relative humidity biases in ERA5 by bivariate quantile mapping: Implications for contrail classification [preprint], EGUsphere, https://doi.org/10.5194/egusphere-2023-2356, 2023a.

https://doi.org/10.5194/egusphere-2024-1361
Preprint. Discussion started: 20 June 2024


Wolf, K., Bellouin, N., and Boucher, O.: Long-term upper-troposphere climatology of potential contrail occurrence over the Paris area derived from radiosonde observations, Atmos Chem Phys, 23, 287–309, https://doi.org/10.5194/ACP-23-287-2023, 2023b.

Wolf, K., Bellouin, N., and Boucher, O.: Distribution and morphology of non-persistent contrail and persistent contrail formation areas in ERA5, Atmos Chem Phys, 24, 5009–5024, https://doi.org/10.5194/ACP-24-5009-2024, 2024.